Journal of Alloys and Compounds 1077 (2026) 189484

Contents lists available at ScienceDirect

Journal of Alloys and Compounds

journal homepage: www.elsevier.com/locate/jalcom

Correlation between structure and magnetic properties for (1-x)$Ba_{0.5}Sr_{0.5}Fe_{12}O_{19}$/(x)$BaZrO_3$ nanocomposites

D. El-Said Bakeer [a,*], Kh. Elaskary [a], Shaimaa A. Habib [a], R. Awad [b], E.M. El-Maghraby [a]

[a] Department of Physics, Faculty of Science, Damanhour University, Damanhour, Egypt
[b] Department of Physics, Faculty of Science, Alexandria University, Alexandria, Egypt

ARTICLE INFO

Keywords:
Magnetic/nonmagnetic nanocomposite
Co-precipitation method
Hexaferrite
Barium zirconate
Magnetic properties

ABSTRACT

In the present study, hard ferromagnetic/non-magnetic nanocomposites with the general chemical formula (1-x) $Ba_{0.5}Sr_{0.5}Fe_{12}O_{19}$/(x)$BaZrO_3$ (BSFO/BZO) have been effectively synthesized using the co-precipitation method coupled with sonication - assisted technique. The XRD technique yielded findings that verified the existence of the individual phases: hexagonal $Ba_{0.5}Sr_{0.5}Fe_{12}O_{19}$ and cubic perovskite $BaZrO_3$, as well as the presence of trace amounts of hematite and ZrO_2. For the BSFO and BZO parent phases, the estimated average crystallite sizes were 53.6 nm and 36.4 nm, respectively. Transmission electron microscopy (TEM) revealed platelet-shaped BSFO particles and quasi-spherical BZO particles, with nanocomposites exhibiting a dual-phase microstructure containing both phases. Grain-size histograms showed two distinct peaks, one for each phase. Selected-area electron diffraction (SAED) confirmed the polycrystalline nature of all samples and verified phase coexistence in the nanocomposites. At higher compositions (x = 0.6 and 0.8), the Debye temperature calculated from the FTIR-active phonon modes increased, owing to improved lattice rigidity. Raman analysis showed that BSFO exhibited distinct metal–oxygen vibrational modes, while BZO displayed defect-related and second-order scattering modes. The peak area analysis suggested that Fe ions were redistributed among the different structural sublattices. This redistribution is likely to play an important role in altering the overall magnetization of the composite material. XPS analysis showed slight shifts of Fe $2p_{3/2}$ and Fe $2p_{1/2}$ to lower binding energies (710.7 and 723.7 eV), indicating a partial reduction of Fe^{3+} to Fe^{2+}. Vibrating sample magnetometry (VSM) results showed that adding nonmagnetic BZO results in a decrease in saturation magnetization (M_s), and remanent magnetization (M_r), subsequently lowering the maximum energy product $(BH)_{max}$. Conversely, the nanocomposite with x = 0.2 exhibited the highest coercivity. Nanocomposites with a low BZO weight percentage are hence more appropriate for use in permanent magnets, motors, and generators. On the other hand, composites with a higher BZO weight ratio are better suited for electromagnetic and thermal management applications, including EMI shielding and filters, cable shielding, and high-temperature capacitors.

1. Introduction

With the progression of technology, there is an increasing need for high-performance materials with exceptional properties. Composite materials, made up of two or more distinct elements, possess unique physical characteristics that surpass those of their individual components. Recently, considerable interest has been focused on nanoscale composites due to their outstanding mechanical, electrical, optical, and magnetic properties, which confer both multifunctionality and enhanced performance [1].

Ferrites are ceramic magnetic oxides that can be grouped based on their chemical formula and crystal structure. These two factors have a direct effect on their magnetic properties and uses. Spinel ferrites with the formula MFe_2O_4 (where M represents Mn, Ni, Zn, Co, ……) usually have good soft-magnetic properties. These materials are characterized by high resistivity, high permeability, low coercivity, and easy magnetization. Because of these properties, ferrites are well-suited for high-frequency, EMI suppression, microwave devices, and biomedical applications [2–4]. Some specific MFe_2O_4 compounds, for example, cobalt ferrite ($CoFe_2O_4$), possess high anisotropy and coercivity and therefore can be used for magnetostriction devices [5]. On the other hand, M-type hexagonal ferrites are conventionally referred to as hard ferrites. They

* Corresponding author.
E-mail address: d_bakeer80@sci.dmu.edu.eg (D.E.-S. Bakeer).

https://doi.org/10.1016/j.jallcom.2026.189484
Received 1 March 2026; Received in revised form 16 June 2026; Accepted 27 June 2026
Available online 30 June 2026

Table 1
Molar quantities of reagents used for the synthesis of $Ba_{0.5}Sr_{0.5}Fe_{12}O_{19}$ and $BaZrO_3$ nanoparticles and their nanocomposites (1-x)$Ba_{0.5}Sr_{0.5}Fe_{12}O_{19}$/(x)$BaZrO_3$.

BZO weight ratio (x)	$BaCl_2.2H_2O$mmol	$SrCl_2.2H_2O$mmol	$FeCl_3.6H_2O$ mmol	$ZrCl_2.8H_2O$mmol
0.0	0.50	0.50	12.0	0.00
0.1	0.55	0.45	10.8	0.10
0.2	0.60	0.40	9.60	0.20
0.4	0.70	0.30	7.20	0.40
0.6	0.80	0.20	4.80	0.60
0.8	0.90	0.10	2.40	0.80
1.0	1.0	0.00	0.00	1.00

are magnetically hard, and this class of oxide materials is generally represented by the chemical formula $MFe_{12}O_{19}$, where M is usually an alkaline earth metal such as Ba^{2+}, Sr^{2+}, Ca^{2+}, or Pb^{2+} [6]. Owing to its distinctive magnetoplumbite structure and inherent magnetic characteristics, it may serve as a future substitute for the limited rare-earth permanent magnets [7]. Out of the hexaferrites, barium and strontium hexaferrites (Ba/Sr)$Fe_{12}O_{19}$ are the most well-studied due to their promising magnetic properties as well as structural stability [8].

$BaFe_{12}O_{19}$ (BFO) is receiving considerable attention in commercial and technological fields due to its scalability, cost-effectiveness, environmental safety, high natural abundance of iron oxide, and distinctive functionality [9]. These advantages arise from its high saturation magnetization, large coercive field, and strong magnetocrystalline anisotropy [10], as well as relatively high Curie temperature (T_C ~720 K) [11] in conjunction with excellent thermal and corrosion resistance [12]. As a result, $BaFe_{12}O_{19}$ has representative applications in the production of permanent magnets, high-density magnetic recording media, microwave and radar-absorbing devices, and energy storage materials, such as supercapacitors [13–16]. Its marked chemical stability also enables its successful incorporation into more complex composite materials for enhanced multifunctional applications.

Although BFO and SFO exhibited ferrimagnetic behavior at room temperature and showed wasp-waisted hysteresis loops, their coercivity (H_c) values were nearly the same. However, SFO displayed higher saturation magnetization (M_s), and remanent magnetization (M_r) than BFO [8]. Despite this, BFO is often favored over SFO because of its superior thermal stability and stronger resistance to demagnetization, whereas SFO is preferred for its lower toxicity. Various researchers have examined the effect of Sr substitution on the structural, magnetic, electrical, and dielectric behavior of M-type hexaferrites with the composition $Ba_{1-x}Sr_xFe_{12}O_{19}$, x = 0, 0.5, and 1 [17–19]. These studies showed that the magnetic properties and electrical conductivity process are strongly reliant on the Sr content.

Although many magnetic materials exhibit outstanding individual properties, no single phase can fully meet the performance criteria required for advanced applications. Consequently, nanocomposites composed of multiple phases with distinct functional characteristics provide a promising route for engineering integrated systems whose overall behavior arises from the complementary properties of the constituent components [20]. Within this framework, numerous studies [21–23] have demonstrated that exchange-spring composites, formed by coupling a high-coercivity hard-magnetic phase with a high-saturation soft-magnetic phase, exhibit cooperative magnetic behavior, resulting in nanocomposites with an enhanced maximum energy product $(BH)_{max}$. Conversely, there have been a limited number of published studies focused specifically on ferromagnetic/non-magnetic perovskite phase composites [24–27]. For example, Manju et al. (2018) [24] studied the magnetic properties of (1-x)$BaSnO_3$/(x)$CoFe_2O_4$ composites prepared by the nitrate method, and they found that increasing ferrite content leads to higher saturation magnetization (M_s), remanence (M_r), and coercivity (H_c). This enhancement is mainly attributed to oxygen vacancies and the formation of F-centers. In contrast, Khirade et al. (2019) [25] observed a decline in magnetic properties in 0.5($BaZrO_3$)/0.5($CoFe_2O_4$) nanocomposites, as $BaZrO_3$ acts as a barrier that weakens magnetic interactions. Dippong et al. [27] synthesized $\delta Zn_{0.5}Ni_{0.5}Fe_2O_4/(100-\delta)SiO_2$ nanocomposites (δ = 0%, 25%, 50%, 75%, and 100%) via the sol–gel method. They found that bulk $Zn_{0.5}Ni_{0.5}Fe_2O_4$ (δ = 100%) exhibited ferromagnetic behavior, whereas pure SiO_2 (δ = 0%) was diamagnetic with only a minor ferromagnetic contribution. In the composites, $Zn_{0.5}Ni_{0.5}Fe_2O_4$ nanoparticles dispersed within the SiO_2 matrix displayed superparamagnetic characteristics. Moreover, both M_s and M_r increased as ferrite concentration increased. The reduction in saturation magnetization at lower ferrite contents was attributed to the SiO_2 coating surrounding the nanoparticles, which enhanced surface spin disorder and decreased the fraction of magnetically active atoms. However, these studies were mainly restricted to spinel ferrites, and the magnetic behavior of composites based on M-type hexaferrites remains largely unexplored.

In this study, a non-magnetic material ($BaZrO_3$) was used as the dielectric matrix and blended with a hard ferromagnetic phase at different weight ratios to form nanocomposites whose physical properties can be tuned. Barium zirconate ($BaZrO_3$) exhibits a highly symmetric cubic phase that remains stable over an unusually wide temperature range of about 4–1600 K without undergoing structural phase transitions [28]. In addition, it exhibits an exceptionally high melting temperature (~2920 °C), minimal thermal conductivity, and remarkable thermal and chemical stability, rendering it suitable for high-temperature applications [29]. Additionally, BZO ceramics demonstrate remarkable dielectric characteristics with a consistent dielectric constant and minimal dielectric loss at microwave frequencies, making them highly desirable for microwave and wireless communication devices like resonators and filters [30,31]. The integration of $BaZrO_3$ with a hard ferromagnetic phase, therefore, creates a strong opportunity to design multifunctional composites in which magnetic, dielectric, and thermal properties can be simultaneously tailored. This synergy is particularly promising for high-frequency microwave devices and electromagnetic interference (EMI) shielding applications.

Nanocomposite ferrite systems can be synthesized via two fundamentally distinct strategies: one-step and two-step synthesis. In one-step synthesis, the ferrite phase and the secondary component (s) are generated simultaneously within a single reaction system, typically via sol–gel, solvothermal, and hydrothermal routes [32–34]. In contrast, the two-step synthesis method involves first preparing the individual parent phases, followed by a secondary step in which these preformed components are combined to form the composite. This second stage involves techniques such as high-speed ball milling, magnetic stirring, and sonication [23,35,36]. Sonication is particularly advantageous, as acoustic cavitation enhances mixing, mass transfer, and diffusion, leading to better dispersion and more uniform nanocomposites [37].

$Ba_{0.5}Sr_{0.5}Fe_{12}O_{19}$ hexaferrites and $BaZrO_3$ perovskites have been widely investigated because of their magnetic and dielectric properties. However, most reported studies have focused on their synthesis, structural features, and functional performance as individual single-phase materials. According to our literature review, no comprehensive study has been performed on nanocomposites using hard magnetic $Ba_{0.5}Sr_{0.5}Fe_{12}O_{19}$ hexaferrite and diamagnetic $BaZrO_3$ perovskite, particularly regarding the influence of $BaZrO_3$ on the structure, surface, and magnetic properties of the composites prepared from such systems. To address the proposed research problem, a series of (1-x)BSFO/(x)BZO

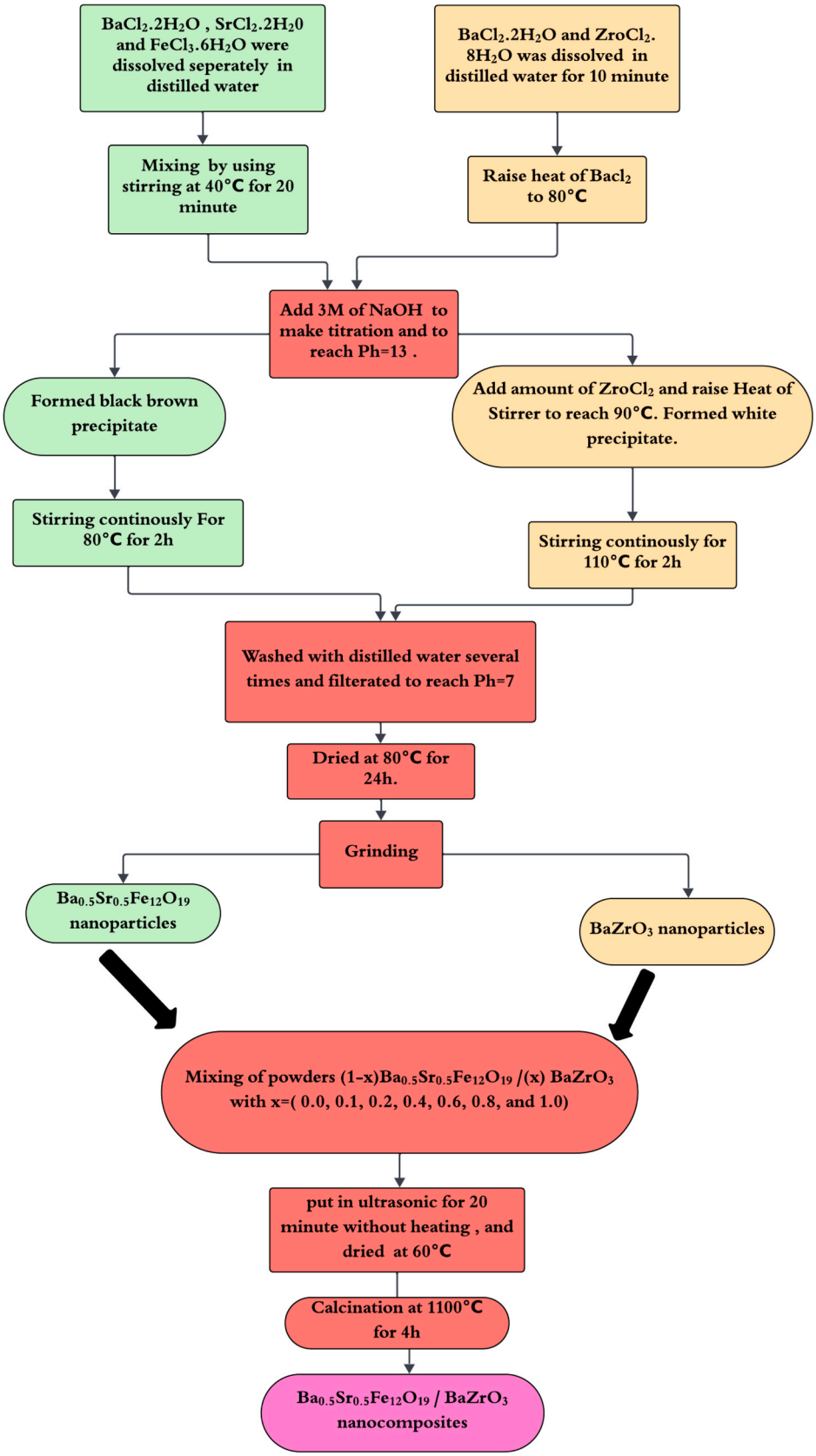

Fig. 1. The diagram illustrating the synthesis of BSFO and BZO nanoparticles and their nanocomposites.

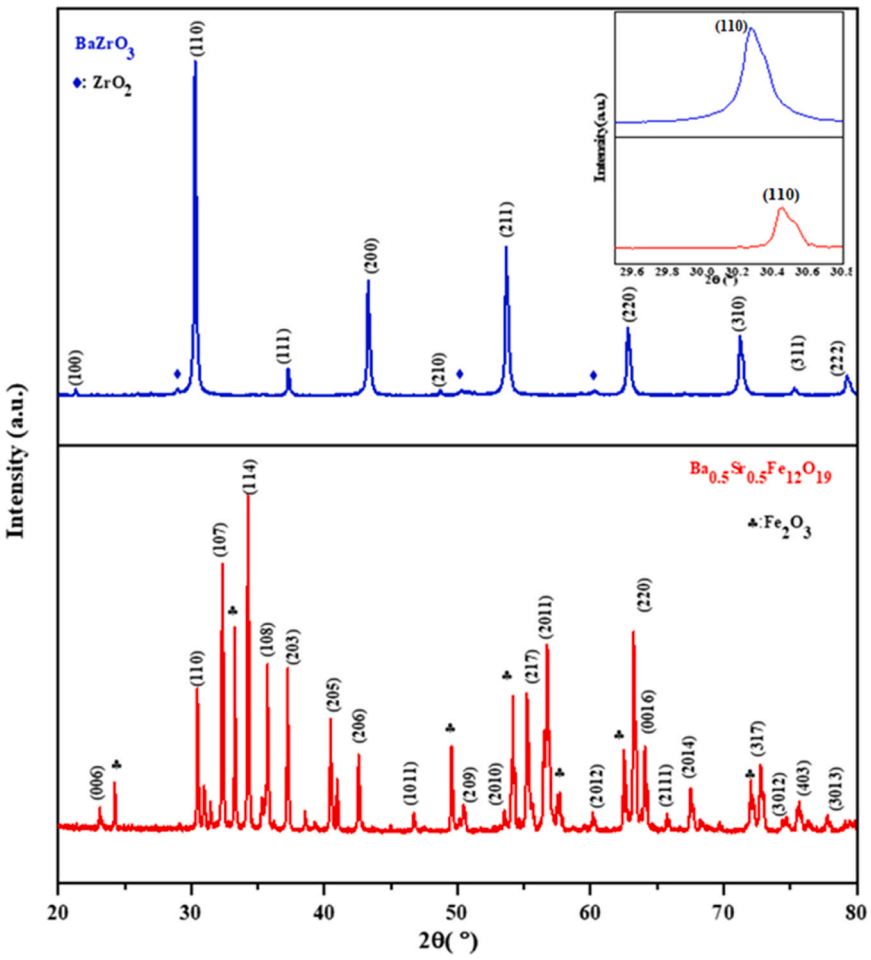

Figure2a. XRD patterns of parent phases $Ba_{0.5}Sr_{0.5}Fe_{12}O_{19}$ and $BaZrO_3$ nanoparticles. The inset provides a magnified view of the main diffraction peaks, corresponding to the (114) plane of BSFO and the (110) plane of BZO.

nanocomposites along with their parent phases, BSFO and BZO were synthesized by coprecipitation and ultrasonication-assisted methods. The structural, surface, morphological, and chemical properties of the samples were extensively characterized by XRD, BET, TEM, FTIR, XPS, and Raman spectroscopy. A vibrating sample magnetometer (VSM) was also used to determine the magnetic characteristics of the prepared samples. The novelty of this particular research is in the relation between composition, structure, and magnetic properties of (1-x)BSFO/(x) BZO nanocomposites, providing new insights into the design of multifunctional magnetic materials for potential technological applications. Further investigations using advanced spectroscopic and impedance methods to analyze the material's dielectric properties and optical characteristics will be valuable for future study.

2. Experimental techniques

Nanocomposites with a chemical formula (1-x)$Ba_{0.5}Sr_{0.5}Fe_{12}O_{19}$/(x) $BaZrO_3$ ((1-x)BSFO/(x) BZO) with x = 0.10, 0.20, 0.40, 0.60, and 0.80 were synthesized by sonication-assisted mixing of $Ba_{0.5}Sr_{0.5}Fe_{12}O_{19}$ and $BaZrO_3$ nanoparticles in their respective weight ratio. Both parent phases were prepared using the co-precipitation technique. Initially, we prepare $Ba_{0.5}Sr_{0.5}Fe_{12}O_{19}$ hexaferrite. To start, we dissolved 1 M $BaCl_2.2H_2O$ and $SrCl_2.2H_2O$ separately in distilled water at 30 °C for 10 min while stirring magnetically. $FeCl_3.6H_2O$ was separately dissolved in distilled water at 30 °C for 15 min. Then, we mixed all three solutions and stirred them at 40 °C for 20 min. Later, we added 3 M NaOH to the solutions slowly dropwise until a pH of 13 was reached, giving rise to dark brown precipitates. The reaction mixture was then allowed to heat up to 80 °C and maintained in this condition for a period of 2 h with constant stirring. To prepare $BaZrO_3$, we dissolved $BaCl_2.2H_2O$ in distilled water using a stirrer and magnet at room temperature, stirring for 10 min, $ZrOCl_2.8H_2O$ in distilled water at 30 °C for a period of 10 min separately. The $BaCl_2.2H_2O$ solution was subsequently heated to 80 °C, and 3 M NaOH was added until the pH reached 13.0. The $ZrOCl_2{\cdot}8H_2O$ solution was then added drop by drop, resulting in the formation of white precipitates. Then, the reaction temperature was subsequently raised to 110 °C and held for 2 h. Ultimately, both precipitates were washed multiple times with deionized water to eliminate leftover salts and subsequently dried at 80 °C for 24 h to remove any remaining moisture. The specific molar quantities of all reagents used to synthesize the parent phases and their nanocomposites are listed in Table 1.

The resultant two powders were ground well and divided into seven groups: $Ba_{0.5}Sr_{0.5}Fe_{12}O_{19}$, $BaZrO_3$, nanocomposites with x = 0.10, 0.20, 0.40, 0.60, and 0.80. To fabricate (1-x)$Ba_{0.5}Sr_{0.5}Fe_{12}O_{19}$/(x)$BaZrO_3$ nanocomposites, stoichiometric amounts of $Ba_{0.5}Sr_{0.5}Fe_{12}O_{19}$ and $BaZrO_3$ precursor powders corresponding to the desired x values were first dispersed in 20 ml of ethanol. The suspensions were sonicated using a high-power ultrasonic probe for a fixed duration of 20 min. This sonication-assisted approach enabled uniform distribution of $BaZrO_3$ within the $Ba_{0.5}Sr_{0.5}Fe_{12}O_{19}$ matrix across all compositions. Following sonication, the mixtures were dried to remove the solvent. Finally, all samples were calcined at 1100°C for 4 h at a rate of 4°C/minute. The diagram illustrating the synthesis of BSFO and BZO nanoparticles and their nanocomposites is depicted in Fig. 1.

To investigate the crystal structures and phase purity of BSFO, BZO,

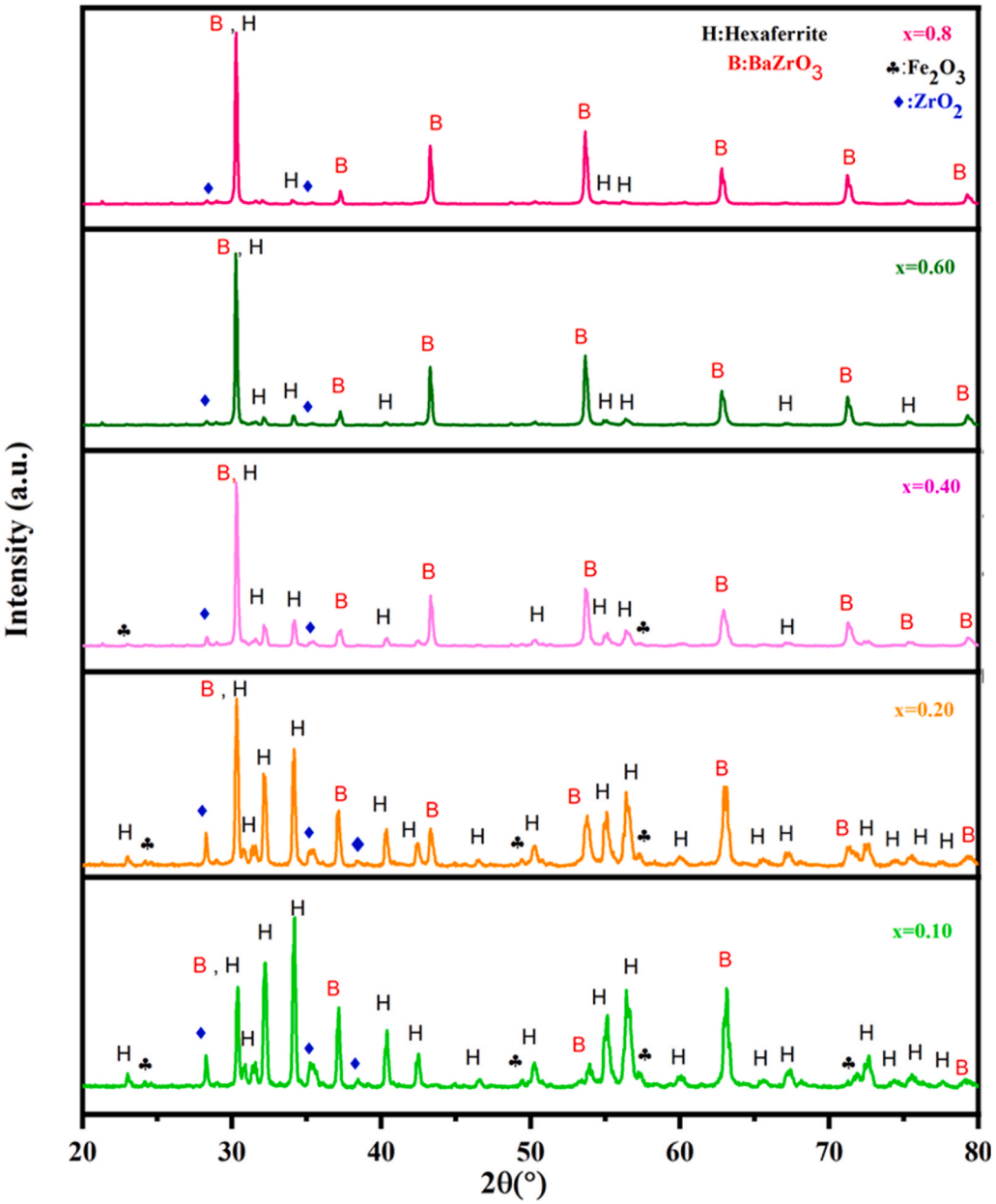

Fig. 2b. XRD patterns of (1-x)BSFO/(x)BZO nanocomposite samples with x = 0.1,0.2,0.4,0.6 and 0.8.

and (1-x)BSFO/(x)BZO nanocomposite samples, X-ray diffraction (XRD) analysis was performed utilizing a Bruker D8 Advance X-ray diffractometer using Cu-Kα radiation (λ = 1.5418 Å). Measurements were performed at a scan rate of 2°/min across a Bragg angle (2θ) range of 10°–80°. Phase identification was conducted using MAUD software, based on the captured diffraction patterns. The specific surface area was determined using the Brunauer–Emmett–Teller (BET) method with a Belsorb III instrument. The samples were degassed at 150 ºC for 3 h before measurement. Surface morphology was analyzed via transmission electron microscopy (TEM) employing a JEOL JEM-100Cx microscope functioning at an accelerating voltage of 80 kV. Particle sizes from TEM images and ring diameters from SAED patterns were measured with ImageJ software. Fourier-transform infrared (FTIR) spectroscopy was utilized for functional group analysis with a Nicolet iS5 spectrometer at ambient temperature within the range of 4000–400 cm^{-1}. Micro-Raman spectroscopy (Renishaw inVia, UK) was used for vibrational analysis of the synthesized samples within the range of 100–3500 cm^{-1} utilizing a 532 nm laser source. X-ray photoelectron spectroscopy (XPS) measurements were performed using a K-Alpha system (Thermo Fisher Scientific, USA) equipped with monochromatic Al Kα radiation. Survey scans were recorded at a pass energy of 200 eV, while high-resolution (narrow) scans were obtained at 50 eV. Before analysis, all elemental spectra were calibrated against the C 1s peak at approximately 285 eV, used as the internal reference. Magnetic measurements at room temperature were performed with a Lakeshore 7410 magnetometer in an applied magnetic field from −20 kG to +20 kG.

3. Results and discussions

3.1. X-ray diffraction analysis (XRD)

X-ray diffraction (XRD) is used to ensure that $Ba_{0.5}Sr_{0.5}Fe_{12}O_{19}$, $BaZrO_3$ nanoparticles, and their nanocomposites are formed successfully. XRD patterns for the parent phases $Ba_{0.5}Sr_{0.5}Fe_{12}O_{19}$ and $BaZrO_3$ are presented in Fig. 2(a). XRD peaks of $Ba_{0.5}Sr_{0.5}Fe_{12}O_{19}$ correspond to M-type hexaferrites with space group $P6_3/mmc$, matching JCPDS# 00-

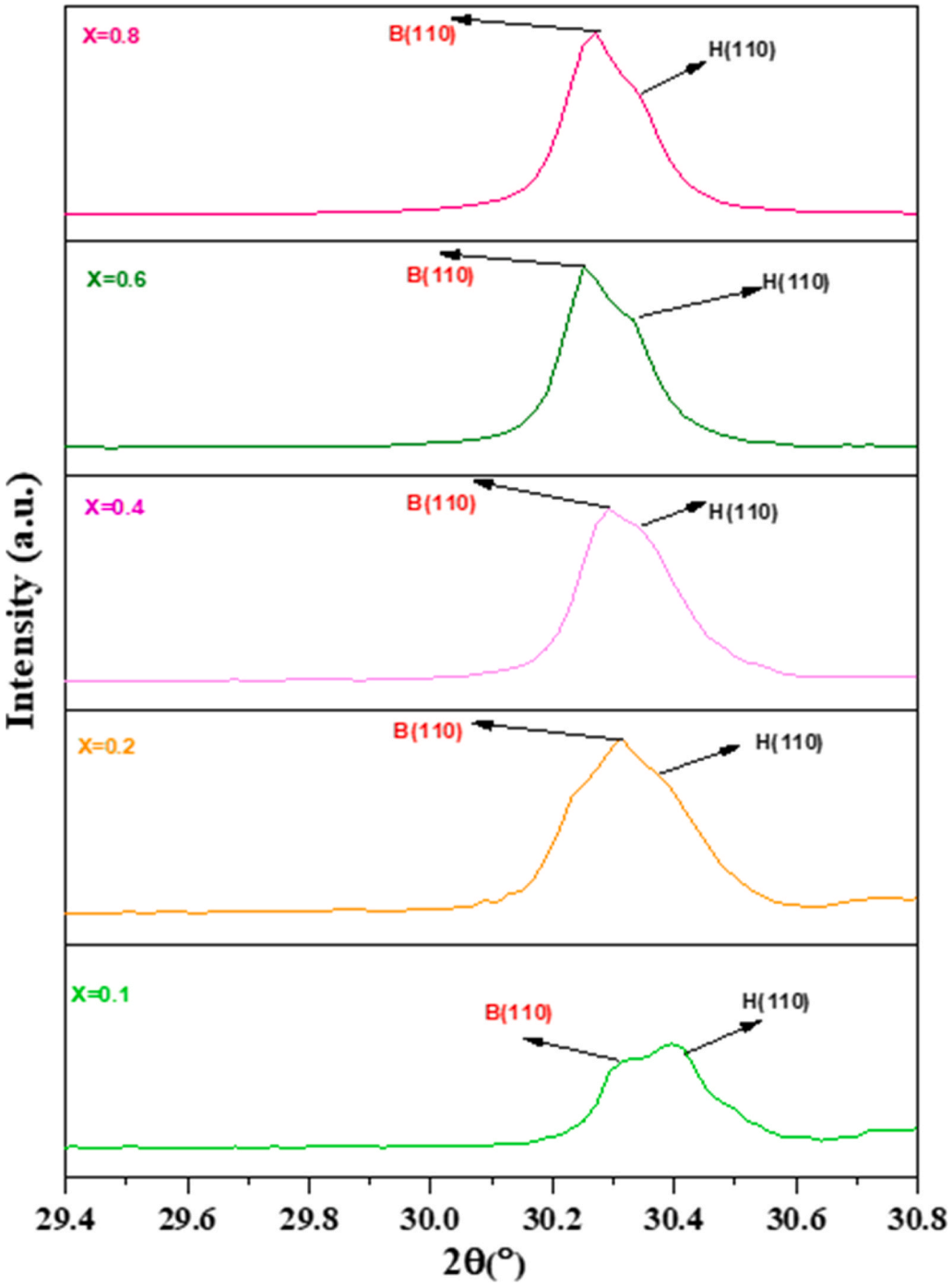

Fig. 2c. Overlapping (110) reflections of $Ba_{0.5}Sr_{0.5}Fe_{12}O_{19}$ and $BaZrO_3$ perovskite phases.

043-0002 [38]. Additionally, a minor trace of secondary phase associated with hematite (Fe_2O_3; JCPDS card no. 33-0664) is observed. The formation of hematite peaks alongside the formation of various hexaferrites has been previously reported [23]. This might be because the excess Fe ions eventually converted to Fe_2O_3 as a result of the loss of Ba and Sr ions during the thermal decomposition process [38].

For $BaZrO_3$, the XRD pattern shows main diffraction peaks at $2\theta = 30.26°, 43.16°, 53.57°, 62.75°$, and $71.17°$. These peaks correspond to the (110), (200), (211), (220), and (310) crystal planes of the cubic perovskite BZO phase with $Pm\bar{3}m$ space group symmetry, in good agreement with the standard JCPDS card No. 06-0399 [29]. A small amount of monoclinic zirconia (ZrO_2) can be observed at $2\theta = 28.98°$, 50.23°, and 60.28° (JCPDS card No.013-0307) [39].

The XRD patterns of nanocomposites (1-x) $Ba_{0.5}Sr_{0.5}Fe_{12}O_{19}$/ (x) $BaZrO_3$ with different weight ratios x = 0.1, 0.2, 0.4, 0.6, and 0.8, are displayed in Fig. 2(b). The diffraction patterns of nanocomposites verify the presence of BSFO and BZO phases, marked with (H) and (B), respectively, with no evidence of chemical interaction between them. This demonstrates how effectively the synthesis process creates nanocomposites while preserving their intrinsic structure. No noticeable shift in the 2θ position of the diffraction peaks for the two phases occurs as the BZO content increases, suggesting minimal diffusion between the two phases [40]. Moreover, XRD patterns of the nanocomposites show a systematic variation in the intensity of both phases with rising weight ratio of BZO, x. As the BZO weight ratio increases, the intensity of the (110) main peak associated with BZO increases, whereas the intensity of

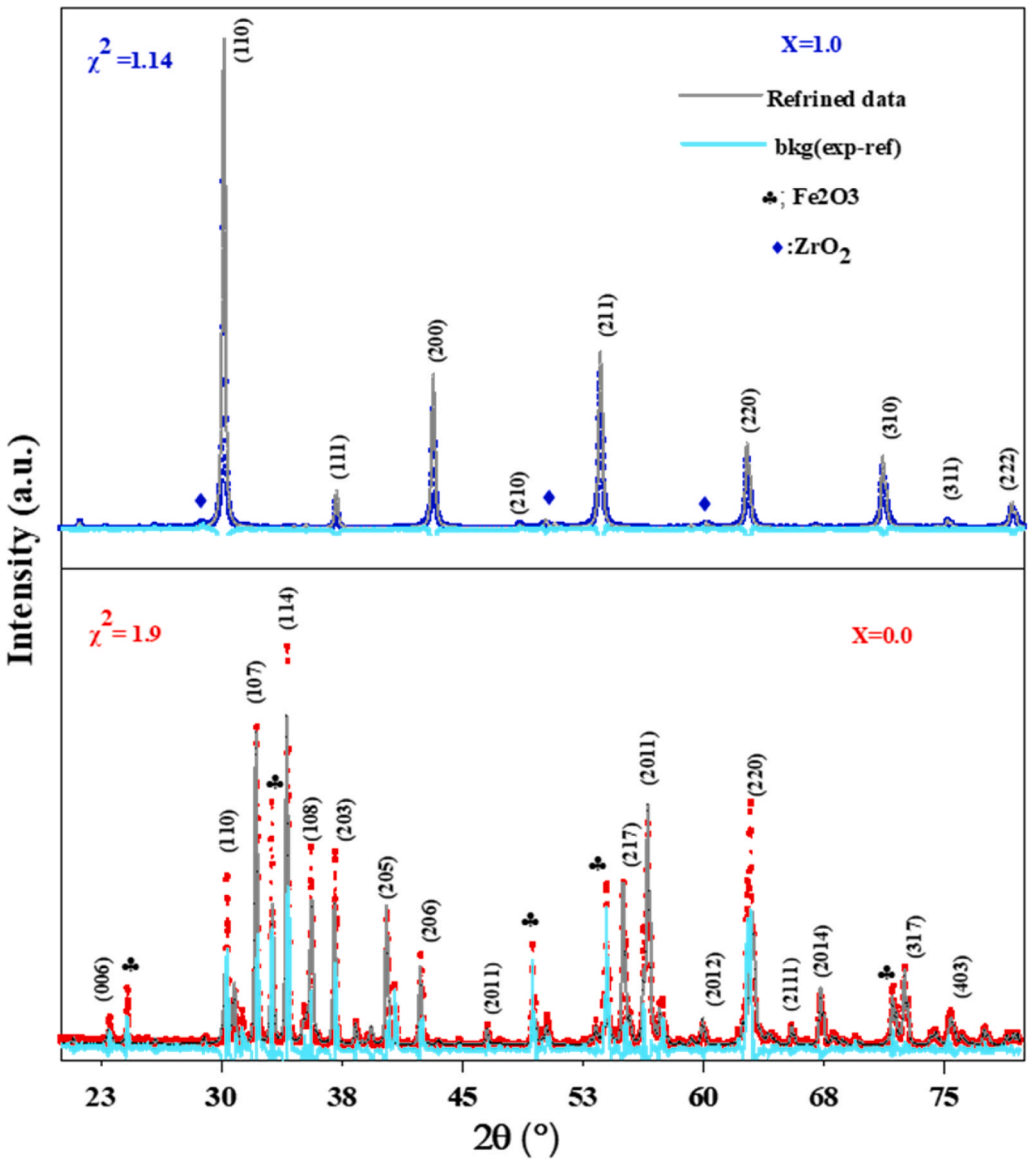

Fig. 3. a: Rietveld refinement of the XRD patterns of (a) $Ba_{0.5}Sr_{0.5}Fe_{12}O_{19}$ and $BaZrO_3$ nanoparticles and (b) (1-x)BSFO/(x)BZO nanocomposite samples.

the (114) peak related to SBFO becomes weaker. This variation in intensity suggests the existence of scattering contributions from both phases, affirming that the distinct phases are effectively integrated within the bi-phase system, a typical trait of any composite [41]. Moreover, the intensity of Fe_2O_3 peaks diminishes as the BZO ratio increases, attributed to the coupling between BZO and BSFO that hinders the loss of Ba and Sr ions [38]. It is worth mentioning that BSFO shows a diffraction peak at $2\theta = 30.34°$, whereas BZO shows its main diffraction peak at $2\theta = 30.147°$, both corresponding to the (110) reflection plane (see the inset of Fig. 2a). This close alignment of diffraction angles suggests partial structural compatibility or the possibility of overlapping reflections between hexaferrite and perovskite phases, as shown in Fig. 2 (c).

Rietveld refinement is applied to the XRD data using MAUD software, enabling quantitative assessment of the XRD patterns and providing reliability indicators such as the goodness factor χ^2. Excellent agreement with the experimental data is indicated by the estimated goodness-of-fit factor, which ranges from 1.02 to 1.20 (Figs. 3(a), 3(b)), thereby ensuring reliable results. Utilizing Maud software, the volume fractions of the two parent phases and the associated impurity phases are estimated and presented in Table 2. As shown in this Table, the composite with a higher BZO weight ratio exhibits a reduction in the volume fraction of the Fe_2O_3 phase, and becomes undetectable in the composites with x = 0.6 and 0.8, signifying enhanced phase purity. Conversely, the volume fraction of ZrO_2 associated with the formation of $BaZrO_3$ shows a minor alteration across the composite samples. Regarding the increase in the volume fraction of BZO phase in the nanocomposites, it is observed that the volume fraction of the hard hexaferrite diminishes steadily from 89.2% (x = 0.1) to 18.9% (x = 0.8), while the volume fraction of the perovskite phase rises from 3.8% (x = 0.1) to 74.2% for x = 0.8. These findings verify that the composites are formed in accordance with the intended phase ratios.

Additionally, the lattice parameters (*a* and *c*) for BSFO and the lattice parameter (a) for BZO are determined for each phase in both the parent samples and the nanocomposite samples, based on the following equations [25,41],

$$d_{hkl} = \left(\frac{4(h^2 + hk + k^2)}{3a^2} + \frac{l^2}{c^2}\right)^{-1/2} \quad (1)$$

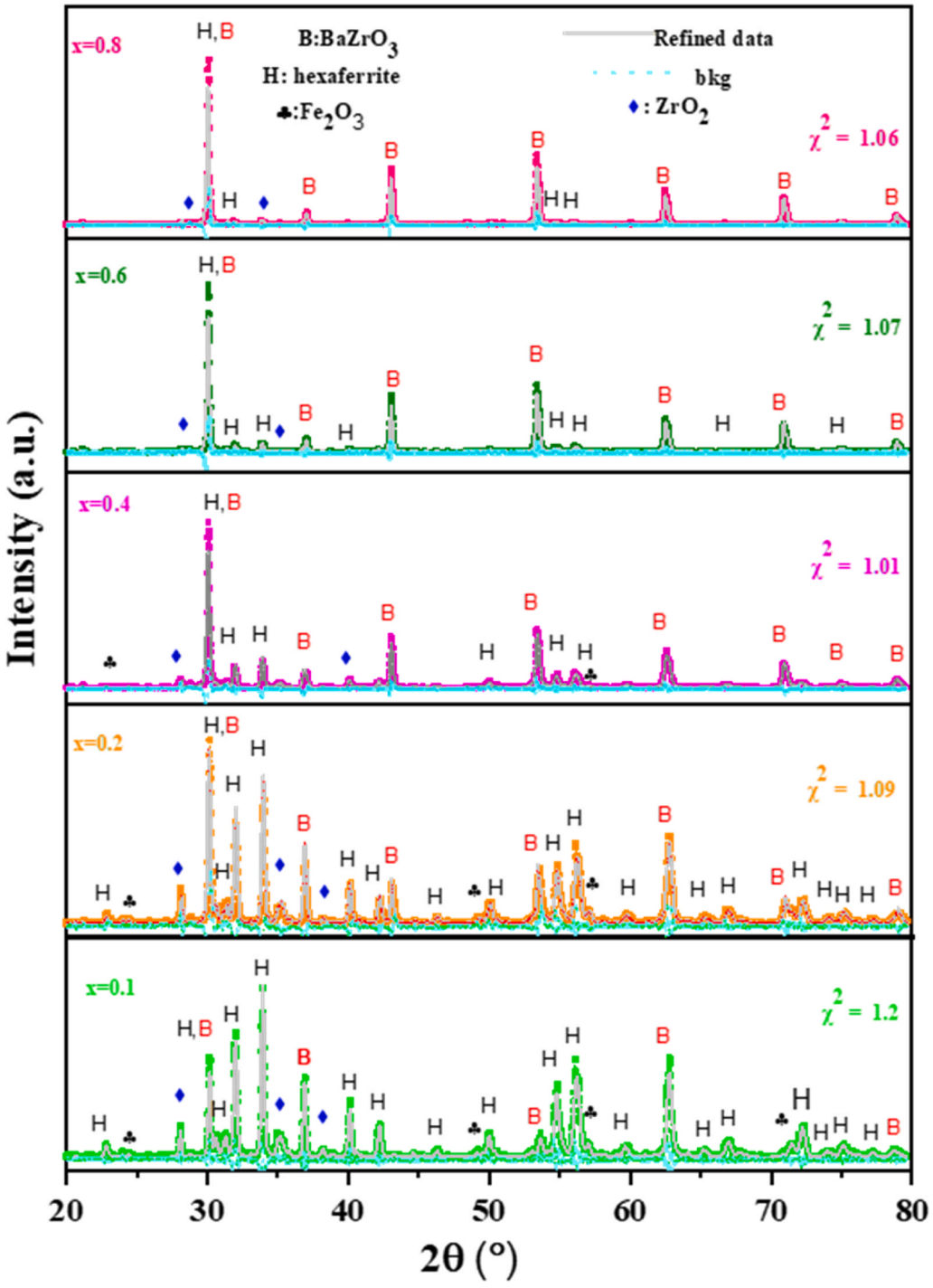

Fig. 3. (*continued*).

$$a = d_{hkl}\sqrt{h^2 + k^2 + l^2} \quad (2)$$

where d_{hkl} is the interplanar distance and (h k l) are Miller indices. The estimated values of the lattice parameters are listed in Table 2. The hexagonal phase has lattice parameters $a = 5.87$ Å and $c = 23.146$ Å, and the lattice parameter (a) of the cubic perovskite is 4.189 Å; both are in good agreement with previously reported values [42]. Lattice parameters' a and c of BSFO increases with growing BZO phase ratio, while the lattice parameter (a) of the BZO phase reduces from 4.189 to 4.177 Å. The slight alteration in the lattice parameters within the composite samples can be attributed to cation diffusion across the interface and the resulting microstrain within the crystal structure [41]. As shown in Table 2, the calculated c/a ratios for BSFO and composite samples range from 3.94 to 3.91, which confirms the formation of an M-type hexagonal structure [43].

Scherrer's equation and Stokes-Wilson (S-W) equation are employed to estimate the average crystallite size (D) and the microstrain (ε) of the individual phases, respectively, based on the following equations [38]:

$$D = \frac{k.\lambda}{\beta \cos\theta} \quad (3)$$

$$\varepsilon = \frac{\beta}{4\tan\theta} \quad (4)$$

Table 2
Lattice parameters and volume fractions calculated for (1-x)$Ba_{0.5}Sr_{0.5}Fe_{12}O_{19}$/(x)$BaZrO_3$ nanocomposites with x = 0.0,0.1,0.2,0.4,0.6, 0.8, and 1.0.

BZO weight ratio (x)	$Ba_{0.5}Sr_{0.5}Fe_{12}O_{19}$					$BaZrO_3$		
	a = b(Å)	c(Å)	c/a	Volume fraction (%)		a (Å)	Volume fraction (%)	
				BSFO	Fe_2O_3		BZO	ZrO_2
0.0	5.87 ± 0.006	23.146 ± 0.06	3.943	90.1	9.9	-	-	
0.1	5.88 ± 0.004	23.150 ± 0.01	3.937	89.2	0.8	4.189 ± 0.002	3.8	6.2
0.2	5.89 ± 0.002	23.182 ± 0.02	3.935	81.5	1.2	4.190 ± 0.002	10.6	6.7
0.4	5.89 ± 0.005	23.185 ± 0.03	3.932	52.9	-	4.187 ± 0.007	41.6	5.5
0.6	5.90 ± 0.007	23.185 ± 0.03	3.929	35.5	-	4.175 ± 0.005	59.5	5.0
0.8	5.94 ± 0.008	23.266 ± 0.05	3.917	18.9	-	4.179 ± 0.002	74.2	6.9
1.0	-	-	-	-	-	4.177 ± 0.003	94.3	5.7

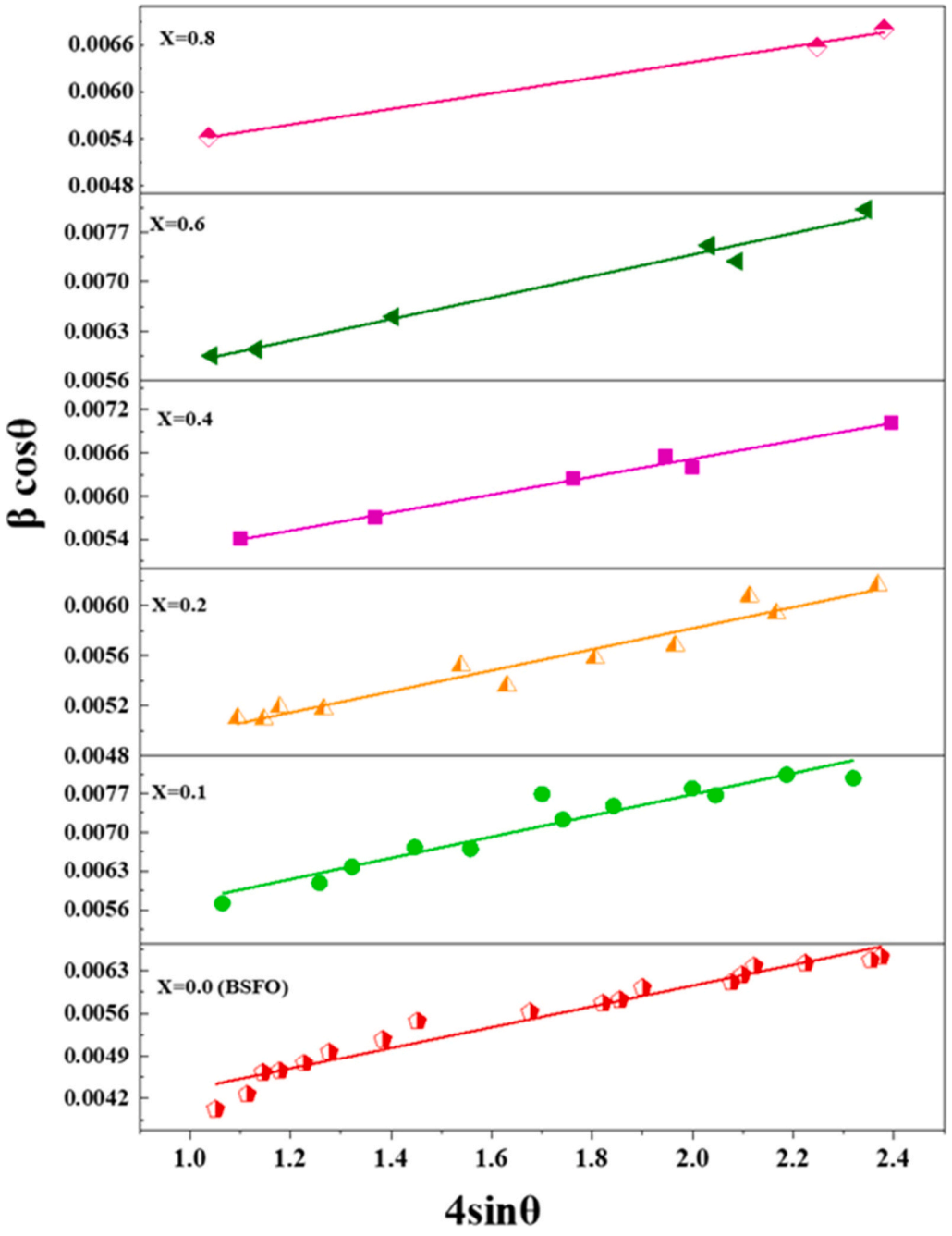

Fig. 4. W–H plots for (a) BSFO and (b) BZO within the (1 −x)BSFO/(x)BZO nanocomposite.

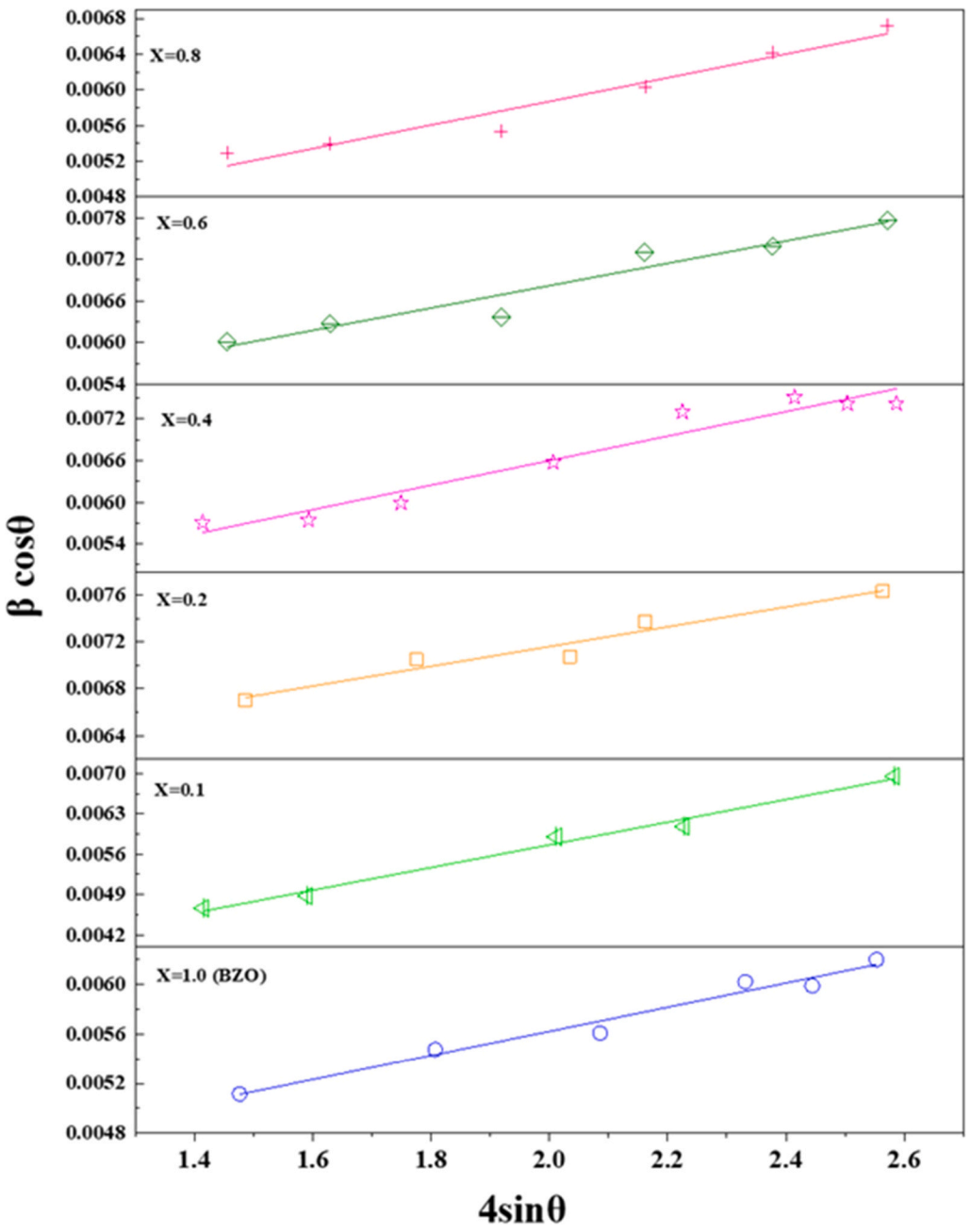

Fig. 4. (*continued*).

Table 3
Crystallite size and microstrain of (1-x)$Ba_{0.5}Sr_{0.5}Fe_{12}O_{19}$/(x)$BaZrO_3$, determined using Scherrer's equation and the Williamson–Hall approach.

BZO weight ratio (x)	Scherrer's equation		Stokes-Wilson equation		Williamson–Hall (W–H) relation			
	Crystallite size (nm)		microstrain× 10^{-3}		Crystallite size (nm)		microstrain× 10^{-3}	
	BSFO	BZO	BSFO	BZO	BSFO	BZO		
0.0	53.6 ± 0.54	-	2.37	-	55.00 ± 3.13	-	1.71	-
0.1	37.9 ± 10	42.3 ± 3.1	4.10	3.39	38.31 ± 3.01	48.11 ± 2.86	1.80	1.53
0.2	36.5 ± 0.47	27.5 ± 3.3	3.99	3.80	37.32 ± 1.25	25.86 ± 0.98	1.12	1.08
0.4	40.8 ± 2.4	32.5 ± 0.65	3.40	3.85	40.00 ± 1.81	34.89 ± 2.20	1.53	1.37
0.6	37.8 ± 3.5	30.0 ± 0.50	2.95	3.20	39.34 ± 2.56	34.97 ± 3.05	2.03	1.41
0.8	47.4 ± 0.69	36.4 ± 2.9	2.98	2.76	45.11 ± 2.84	39.45 ± 2.78	1.88	1.16
1.0	-	35.9 ± 2.1	-	2.72	-	39.35 ± 1.82		2.30

where λ is the wavelength of the Cu-Kα radiation (1.5406 Å), k is a shape factor with a typical value of 0.9, 2θ is the diffraction angle, and β is the full width at half maximum of the main peaks. For the parent phases, BSFO and BZO, the crystallite sizes are 53.60 nm and 36.40 nm,

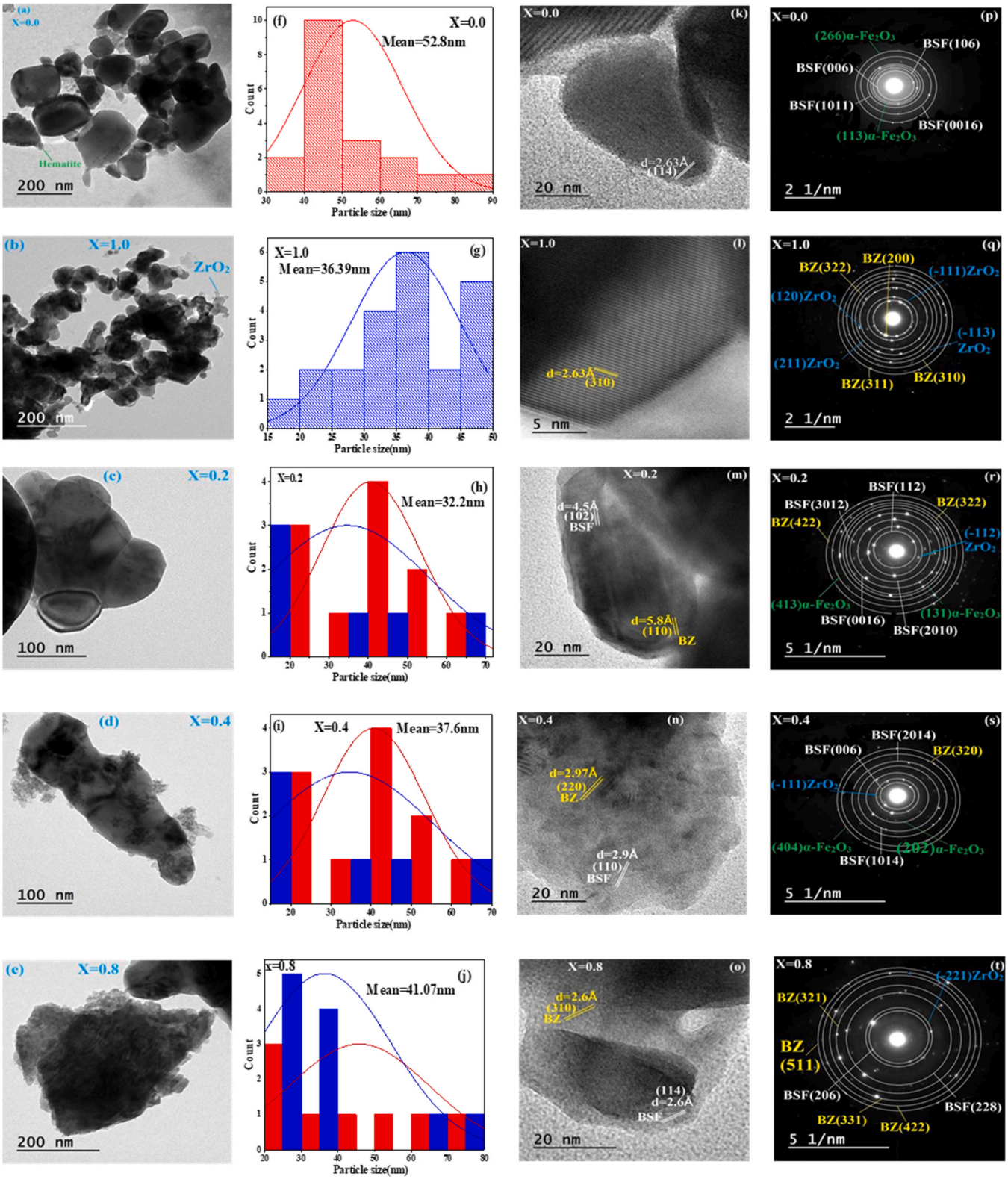

Fig. 5. (a–e) TEM images, (f–j) particle size distribution, (k–o) high-resolution TEM image, and (p–t) SAED patterns for BSFO and BZO nanoparticles and their nanocomposites with x = 0.2, 0.4 and 0.8.

respectively. In addition, the crystallite sizes of BSFO and BZO are also determined in the composite samples.

For deeper analysis of crystallite size and microstrain, the Williamson–Hall (W–H) method [44] is widely used because it provides a more complete picture, capturing both crystallite size and lattice strain, as described in Eq. (5).

$$\beta\cos\theta = \frac{k\lambda}{D_{W-H}} + 4\varepsilon\sin\theta \tag{5}$$

where D_{W-H} and ε correspond to the crystallite size and microstrain,

Table 4
Mean particle size estimated from TEM, the wave number υ_1, υ_2, corresponding to different vibrations and Debye temperature of (1-x)$Ba_{0.5}Sr_{0.5}Fe_{12}O_{19}$/(x) $BaZrO_3$ nanocomposites.

BZO weight ratio (x)	TEM		FTIR		
	Mean particle size		υ_1 cm^{-1}	υ_2 cm^{-1}	Debye temperature (Θ_D) K
	BSFO	BZO			
0.0	52.80 ± 2.24	-	594.28	441.45	744.689
0.1	-	-	591.39	440.38	741.843
0.2	36.06 ± 1.87	28.30 ± 1.45	589.15	441.40	740.965
0.4	40.65 ± 2.54	34.67 ± 1.76	574.85	440.37	729.943
0.6	-	-	567.28	-	815.749
0.8	45.83 ± 3.27	36.30 ± 3.56	562.29	-	808.573
1.0	-	36.39 ± 2.49	556.47	-	800.204

Table 5
The d_{hkl} values estimated from XRD and SAED patterns.

BZO weight ratio (x)	(***hkl***)	d_{hkl} (Å) estimated from XRD	d_{hkl} (Å) estimated from SAED
0.0	(006)	3.857	3.811
	(106)	3.07	3.23
	(1011)	1.947	1.910
	(0016)	1.446	1.445
0.2	(110): BSFO	2.945	2.905
	(311): BZO	1.263	1.263
	(111): BZO	2.419	2.407
	(210): BZO	1.873	1.852
0.4	(217): BSFO	1.667	1.658
	(2111): BSFO	1.423	1.424
	(100): BZ	4.187	4.049
	(111): BZO	2.417	2.410
	(200): BZO	2.093	2.073
	(311): BZO	1.262	1.264
0.8	(226): BSFO	1.386	1.362
	(111):BZO	2.412	2.319
	(222): BZO	1.206	1.176
	(211): BZO	1.706	1.723
1.0	(200)	2.09	2.03
	(310)	1.32	1.34
	(311)	1.26	1.24
	(322)	1.01	1.06

respectively.

For the most intense peaks of BSFO and BZO nanoparticles, $\beta\cos\theta$ are plotted against $4\sin\theta$, as seen in Figs. 4a and 4b, respectively. The average crystallite size is estimated from the y-intercept, while the slope of the fitted line gives the strain value. As observed from Table 3, the crystallite size estimated from the Williamson–Hall (W–H) relation is often slightly smaller than that obtained using the Scherrer equation because the W–H method explicitly accounts for both crystallite size broadening and lattice strain broadening, whereas the Scherrer equation assumes that peak broadening arises solely from finite crystallite size.

The average crystallite size of the BSFO component in the composites is less than that of the parent phase, as seen in Table 3. This reduction is not entirely uniform, with the nanocomposite with x = 0.20 exhibiting the smallest crystallite size. This behavior can be attributed to the heterogeneous distribution of the secondary phase, particle agglomeration, and diffusion-limited grain boundary mobility. In particular, the secondary minor phases might apply a pinning effect, which obstructs the movement of grain boundaries and restricts their grain growth [45]. In addition, the composites exhibit a non-uniform distribution of microstrain, which further contributes to the irregular changes observed in crystallite size.

3.2. Transmission electron microscope (TEM)

A comprehensive TEM analysis is conducted to gain a better understanding of the microstructure of the synthesized samples. TEM images of $Ba_{0.5}Sr_{0.5}Fe_{12}O_{19}$ and $BaZrO_3$ nanoparticles calcined at 1100 °C for 4 h are presented in Figs. 5(a) and 5(b), respectively. The BSFO sample exhibits platelet-shaped particles with a clear hexagonal form, along with smaller spherical particles associated with Fe_2O_3. In comparison, BZO particles exhibit a mostly quasi-spherical shape with significant agglomeration. The observed clustering in BSFO parent phase can be ascribed to the magnetic interaction among particles. Such agglomeration is frequently observed, particularly in materials synthesized at high temperatures [46].

As illustrated in Fig. 5(c–e), the nanocomposite samples (1-x)BSFO/(x)BZO with x = 0.2, 0.4, and 0.8 exhibit a dual-phase structure, consisting of both BSFO and BZO phases. As BZO weight ratio increases, its particles tend to cluster with the hexaferrite particles, and the particles stack together [47]. This diminishes the uniformity of the interfaces and likely weakens the exchange coupling between hexaferrite grains. This behavior aligns with the reduction in magnetization reported in Section 3.7. The change in microstructure of the composites from that of the parent samples is due to strain induced by the incorporation of BZO [48]. The thermodynamic stability of the perovskite phase introduces additional strain at the BSFO grain boundaries, which suppresses diffusion during calcination, leading to reduced particle size and modified morphology.

The mean particle size is determined by applying Gaussian fitting to the size distribution histograms, Fig. 5f–j, acquired through ImageJ software. Histogram analysis shows average particle size of 52.8 nm for BSFO and 36.39 nm for BZO, which are comparable with the results obtained from the XRD analysis. It is pertinent to mention here that the existence of two peaks in the histograms of nanocomposites establishes the coexistence of BSFO and BZO phases. The average sizes of both parent phases in the nanocomposite samples are also analyzed and are presented in Table 4, which shows comparability with the values estimated using the Scherrer equation.

A comprehensive investigation of the microstructure of the synthesized samples is conducted through HRTEM/SAED analyses. The HRTEM images of BSFO and BZO in Figs. 5(k)and 5(i), display the lattice fringes linked to the (114) planes of BSFO hexagonal structure phase and (310) plane of BZO perovskite structure phase, with interplanar spacings of 2.63 Å and 2.60 Å, respectively. The D-values of the lattice fringes in the HRTEM images of the two parent phases match the values derived from the X-ray diffraction patterns. HRTEM images of (1-x)BSFO/(x) BZO nanocomposites for x = 0.2, 0.4, and 0.8 (Fig. 5m–o) reveal two distinctly identifiable sets of lattice fringes at the interface. As observed, the two phases are separated by a well-bonded boundary, indicating the possibility for lattice adjustment [41]. These observations confirm the coexistence of both BSFO and BZO phases within the nanocomposite samples.

The selected-area electron diffraction (SAED) patterns of the synthesized samples (Fig. 5(p–t) show distinct, spotty ring characteristics, signifying their polycrystalline structure. Values of interplanar spacing (D-spacing) are derived from the diameters of the concentric diffraction rings seen in the SAED patterns, and closely match those obtained from X-ray diffraction (XRD), as detailed in Table 5. Figs. 5(p) and 5(q) display the SAED patterns of the parent phases BSFO and BZO, with the set of diffraction rings corresponding to the hexagonal structure of BSFO and BZO phases, respectively. In addition, diffraction rings associated with Fe_2O_3 and ZrO_2 are observed in the SEAD pattern for BSFO and BZO, respectively, aligning with the findings from the XRD analysis. The SAED patterns for nanocomposites exhibit two distinct sets of diffraction

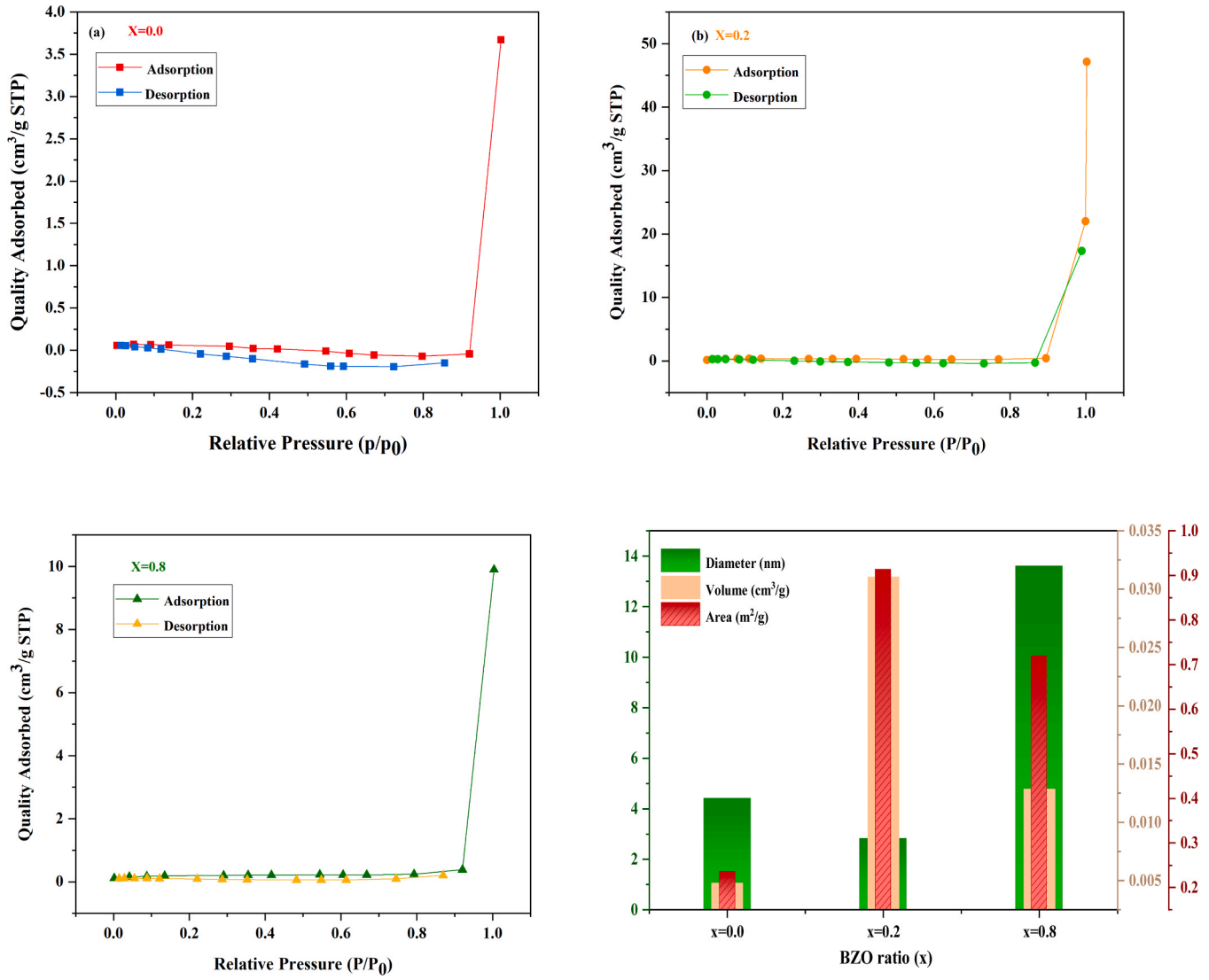

Fig. 6. (a) N_2 adsorption-desorption isotherms and (b) variation of surface area, pore volume, and pore diameter of $Ba_{0.5}Sr_{0.5}Fe_{12}O_{19}$, $BaZrO_3$ nanoparticles, and (1-x)BSFO/(x)BZO nanocomposite with x = 0.2.

spots, as shown in Fig. 5(r–t). One set can be indexed to the hexagonal BSFO crystal structure, while the other corresponds to the cubic perovskite phase BZO.

3.3. Surface area measurements

Nitrogen adsorption–desorption experiments are conducted to evaluate the textural properties of the synthesized (1-x)BSFO/(x)BZO nanoparticles. The Barrett–Joyner–Halenda (BJH) method is employed to calculate the pore volume and diameter, while Brunauer–Emmett–-Teller (BET) analysis is utilized to assess the surface area. Fig. 6(a–c) present the N_2 adsorption–desorption isotherms obtained for the samples with x values of 0.0, 0.2, and 0.8. Based on the IUPAC classification, the sample exhibited a mesoporous structure characterized by a type IV adsorption-desorption isotherm [49]. A distinct H3-type hysteresis loop observed within the relatively high-pressure P/P_0 range of 0.0–0.9 suggests the existence of slit-shaped mesopores, likely resulting from the agglomeration of particles [50], which is also confirmed by HR-TEM Images. The initial segment of the IV isotherm aligns with the pattern observed in type II isotherms, which depict unrestricted monolayer-to-multilayer adsorption [50]. Fig. 6d illustrates how the surface area, pore volume, and pore diameter change in relation to the concentration of BZO. The Barrett-Joyner-Halenda (BJH) average pore size for all the samples is determined to be within the range of 2.8–13.6 nm, which indicates that the materials are mesoporous in nature. Furthermore, the surface area of the 20% BSFO/BZO composite increases with a decrease in the average pore size. This phenomenon occurs because crystallinity and particle size are inversely related to surface area. As revealed by the XRD analysis, the 20% BSFO/BZO has a smaller crystallite size, so have larger surface area. This significant increase in surface area indicates that 0.8BSFO/0.2BZO nanocomposite exhibits enhanced catalytic potential when compared to other samples.

3.4. FTIR analysis

The FTIR spectra for $Ba_{0.5}Sr_{0.5}Fe_{12}O_{19}$, $BaZrO_3$, and their nanocomposites are shown in Fig. 7. The distinctive peaks of $Ba_{0.5}Sr_{0.5}Fe_{12}O_{19}$ appear at 441 and 594 cm^{-1} [51]. These peaks result from the unequal Fe–O stretching vibrations at both tetrahedral and octahedral locations. In addition, the absorption band around 858 cm^{-1} is linked to Ba–O stretching vibrations [39]. Conversely, the primary absorption peak of $BaZrO_3$ is noted at 557.46 cm^{-1}, related to the stretching of Zr–O bonds within the octahedral positions of the perovskite framework. Hence, this band corresponds to Zr^{4+}ions in octahedral coordination and

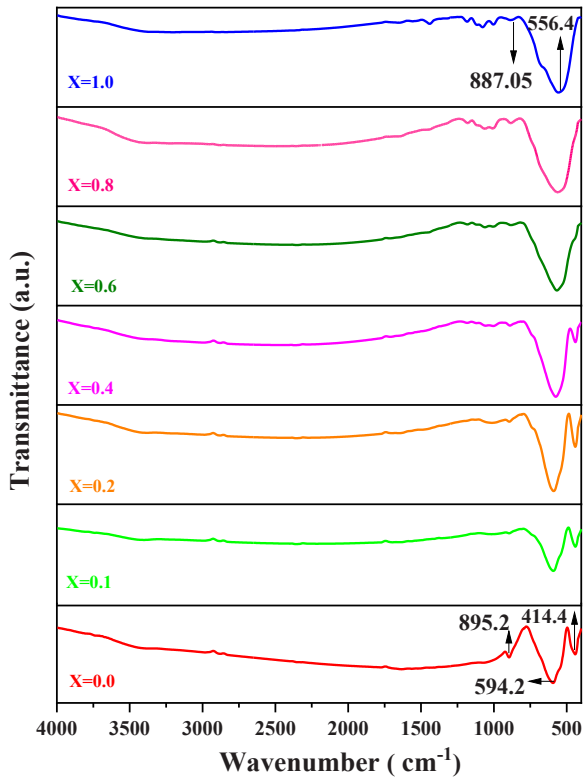

Fig. 7. FTIR spectrum of BSFO and BZO nanoparticles and their nanocomposites.

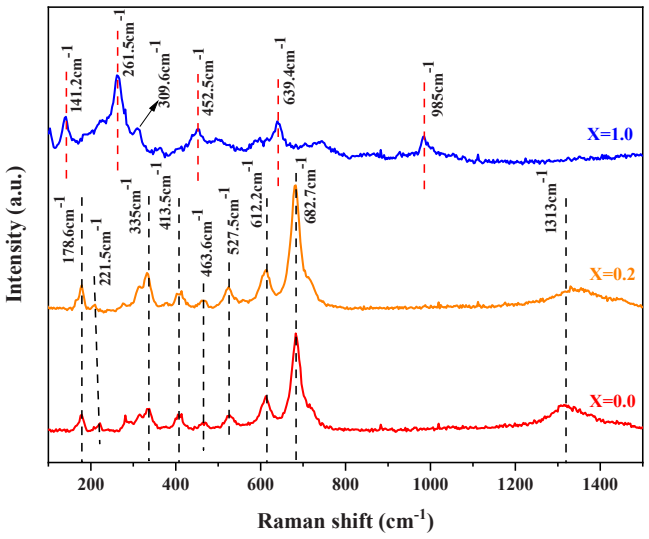

Fig. 8. Room temperature Raman spectra of parent phases $Ba_{0.5}Sr_{0.5}Fe_{12}O_{19}$ and $BaZrO_3$ nanoparticles and nanocomposite of (1-x)BSFO/(x)BZO nanocomposite with x = 0.2.

the asymmetric stretching of [ZrO_6] octahedra within the cubic $BaZrO_3$ structure [52]. Furthermore, the stretching vibration modes of OH in water molecules adsorbed on the sample surfaces are observed as a broad band near 3440 cm^{-1} and 1633 cm^{-1} [53]. Table 4 illustrates that the stretching frequency ν_1 is observed to be lower in composites with higher $BaZrO_3$ weight ratios. Moreover, the peak at 441.45 cm^{-1} shifts slightly to a lower value and disappears in composites with higher $BaZrO_3$ ratios (x = 0.6 and 0.8). This variation is a logical consequence of the increases in the $BaZrO_3$ ratio and aligns with the changes in lattice

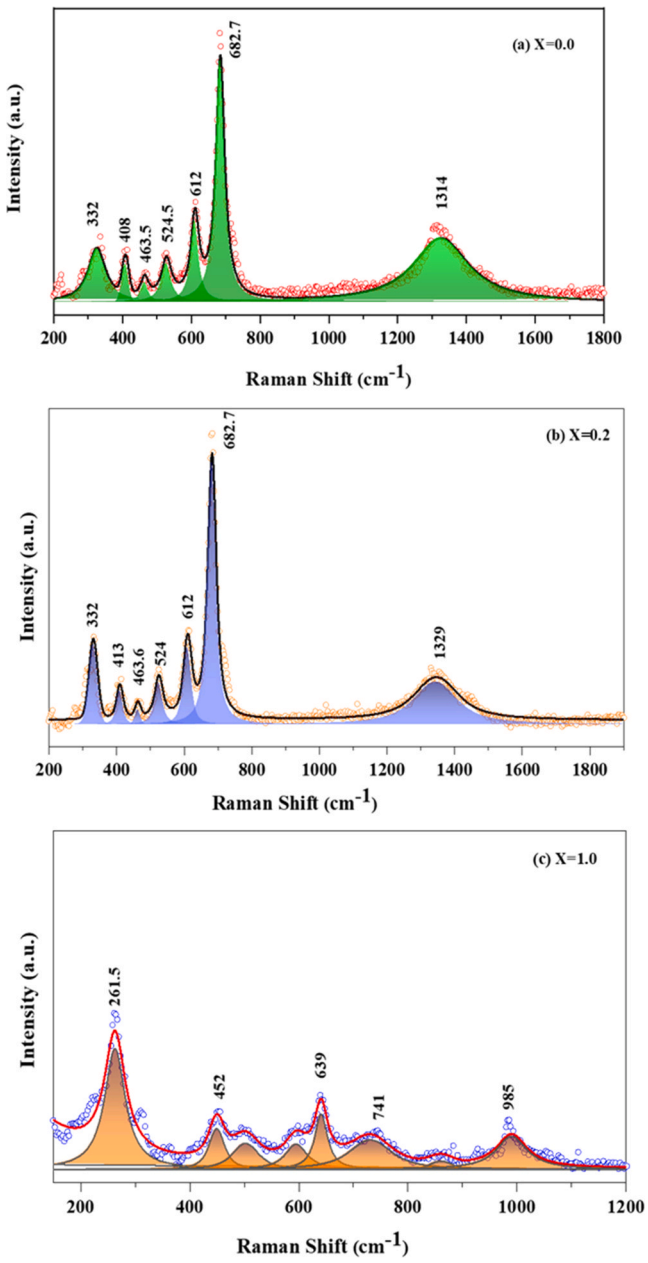

Fig. 9. Room temperature deconvoluted Raman spectra of (a) BSFO (b) 0.8BSFO/0.2BZO (c) BZO.

parameter.

The Debye temperature (Θ_D) is fundamentally related to the maximum phonon frequency (Debye frequency), which represents the upper limit of lattice vibrational modes in a solid.

Estimating (Θ_D) from the characteristic vibrational (phonon) frequency associated with metal–oxygen lattice modes is physically justified according to the following relation [54].

$$\Theta_D = \hbar \frac{\mathbb{C}\nu}{k_B} \tag{6}$$

Where $\omega_D = 2\pi\mathbb{C}\nu$, $\mathbb{C}$ is the velocity of light, k_B is the Boltzmann constant and ν is the mean wave number of the main vibrational modes.

As shown in Table 4, the parent materials BSFO and BZO have Debye temperatures of 744.69 K and 800.20 K, respectively. The Debye temperature of BSFO closely matches earlier experimental results for $BaFe_{12}O_{19}$ (739.613 K) derived from active phonon modes in FTIR spectra [55]. For $BaZrO_3$, the derived Debye temperature aligns with

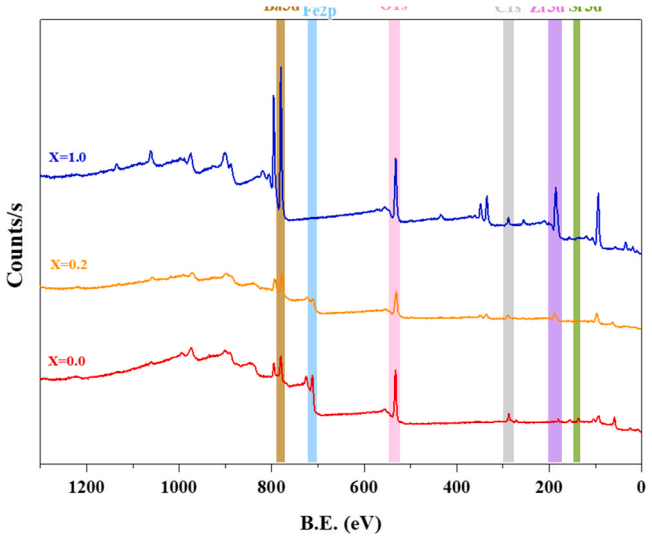

Fig. 10. XPS spectra of (1-x)BSFO/(x)BZO, x = 0.0, 0.2 and 1.0.

that of anion sublattice vibrations (730 K), as the vibrations of the oxygen sublattice are most significant at higher phonon frequencies [56]. Differences between FTIR-derived Debye temperatures and those obtained from heat capacity fitting [57], 525 K, are expected because heat capacity methods include the full phonon spectrum, especially acoustic modes, while FTIR mainly reflects optical phonons. As observed, Debye temperature of the nanocomposites decreases with increasing BZO content up to x = 0.4 due to enhanced phonon scattering at interfacial boundaries. Then increases at higher BZO ratios (x = 0.6 and 0.8) as the stiff perovskite structure of BZO becomes dominant. This increase reflects improved mechanical rigidity and thermal stability, making these composites suitable for thermal barrier coatings and high-temperature capacitor applications.

3.5. Raman spectroscopy

Raman spectroscopy is an analytical non-destructive method that offers insights into crystal structure via molecular vibrational and rotational spectra [58]. According to the group theoretical analysis of hexagonal ferrites, which relies on D6h symmetry. The crystal structure of $BaFe_{12}O_{19}$ exhibits 42 Raman-active modes (11 A_{1g} + 14 E_{1g}+ 17 E_{2g}). In addition, 30 infrared-active modes are expected (13 A_{2u} + 17E_{1u}). The remaining 54 modes (3 A_{1u} + 4 A_{2g} + 13 B_{1g} + 4 B_{1u} + 3 B_{2g} + 12 B_{2u} + 15 E_{2u}) are inactive in both Raman and infrared spectra and are therefore considered silent [59]. In this study, 11 Raman peaks for the BSFO compound are noted and illustrated in Fig. 8. Our results are consistent with previous similar findings [60,61].

The Raman spectra are analyzed and indexed, with the observed vibrational modes detected at approximately 720, 684, 528, 468, 420, 385, 337, 284, 213, 183, and 171 cm^{-1} closely matching those expected for the magnetoplumbite structure [61]. The vibrations of the entire spinel block and octahedral 2a site corresponding to the low-frequency Raman modes at 178.6 and 221.5 cm^{-1} are assigned to E_{1g} symmetry [62]. The notably weak active mode observed at 281.3 cm^{-1} serves as a signature of the vibration at the octahedral 2a site due to A1g symmetry [62]. The E_{1g} and E_{2g} symmetries result in Raman-active modes at 408 and 335 cm^{-1}, respectively, corresponding to vibrational motions of the octahedral 12k site [62]. In addition, a Raman-active mode detected at 465 cm^{-1} is assigned to the A1g symmetry. Raman-active mode identified at 524 cm^{-1} is a result of the vibrations of metal–oxide bonds in the octahedral 12k and 2a sites. This mode is thus called a mixed mode, arising from E_{1g} symmetry [59]. The low vibrational mode detected at 611 cm^{-1} relates to the stretching vibration of the Fe–O bond at the octahedral ($4f_2$) site, aligning with A_{1g} symmetry. As depicted in Fig. 8, the strongest vibrational mode occurs at 694 cm^{-1}, accompanied by a shoulder around 730 cm^{-1}. The A_{1g} mode at 694 cm^{-1} is associated with Fe–O bond vibrations in the FeO_5 bipyramidal units, while the shoulder peak near 720 cm^{-1} is linked to A_{1g} vibrations of Fe–O bonds at the tetrahedral $4f_1$ site [63]. Additionally, the mode observed at 1320 cm^{-1} originates from the vibrations of the tetrahedral ($4f_1$) site [60].

Although first-order Raman-active phonons are not permitted in the cubic perovskite structure, observed Raman spectra of BZO show multiple distinct peaks linked to first-order Raman activity [64]. Conflicting interpretations regarding the origin of these peaks have been present in the prior literature [53,65]. Recent studies [66,67] have sought to address this controversy by proposing that the observed Raman activity originates from defect-induced local distortions of the crystal symmetry. In perovskite materials, such first-order Raman-active modes arise from deviations from centrosymmetry caused by defects such as oxygen vacancies (VO), grain boundaries, lattice strain, and impurities [68]. Karan et al. [69] view the noticeable difference between Raman and X-ray findings as a result of the distinct coherence lengths and timescales that these methods investigate. A small local deformation of the oxygen octahedra can modify Raman selection rules, resulting in the emergence of broad weak bands in the Raman spectrum. From a different viewpoint, Xin et al. [70] propose that the Raman spectra of $BaZrO_3$ are generally understood through second-order scattering processes that involve the interaction of two phonons.

As displayed in Fig. 8, the Raman spectrum for $BaZrO_3$ revealed bands (around ~277, 352, 462, 644, 707, 739, 846, and 1016 cm^{-1}) that align with previous research [52,71]. In particular, the band around 140 cm^{-1} is associated with the movement of Ba atoms in relation to the ZrO_6 octahedra. Conversely, the band near 350 cm^{-1} mainly pertains to twisting and antisymmetric breathing modes of the ZrO_6 octahedron. The band at 691.02 cm^{-1} signifies the movement of apical oxygen atoms in relation to the in-plane oxygens. All of these modes are linked to distortions occurring at the zirconium octahedral site in the $BaZrO_3$ structure [67]. Moreover, the vibrational mode detected at approximately 842 cm^{-1} is associated with the vibrations of O^{2-} ions at the O(6i) sites [71]. Additionally, second-order modes are identified at frequencies of approximately 224.58 and 412.04 cm^{-1} [70]. For the nanocomposite with x = 0.2, the major Raman peaks are associated with BSFO, with minor peaks related to BZO, due to the dominant volume fraction and higher Raman scattering cross-section of the BSFO phase, while the BZO phase is present in a smaller proportion and/or exhibits weaker Raman activity. Raman analysis confirms that the BSFO and BZO crystal phases do not undergo a chemical reaction in the composite. The Raman spectra are deconvoluted into individual Lorentzian peaks, as shown in Fig. 9(a–c), and the areas under these peaks were calculated. The results show that the Raman bands at 332 and 408 cm^{-1} show a reduction in area for the sample with x = 0.2, suggesting a weakening of the FeO_6 octahedral vibration modes at the 12k sites. On the other hand, the bands at 612 and 682 cm^{-1} show an increase in area, indicating a relative strengthening of Fe–O stretching vibrations at both the octahedral ($4f_2$) and tetrahedral ($4f_1$) sites. This behavior is attributed to a redistribution of Fe ions between the different sublattices within the structure. Such redistribution is expected to significantly influence the net magnetization of the composite sample, as further discussed in Section 3.7.

3.6. X-ray photoelectron spectroscopy (XPS)

XPS is used to gain deeper insights into the elemental states and chemical composition of the composite material by evaluating binding energy values. The survey spectrum of the (1-x)BSFO/(x)BZO nanocomposites, with x = 0.0, 0.2, and 1.0, is displayed in Fig. 10, distinctly highlighting the characteristic photoelectron peaks corresponding to Ba 3d, Sr 3d, Zr 3d, Fe 2p, and O 1s. This confirms the chemical purity of the

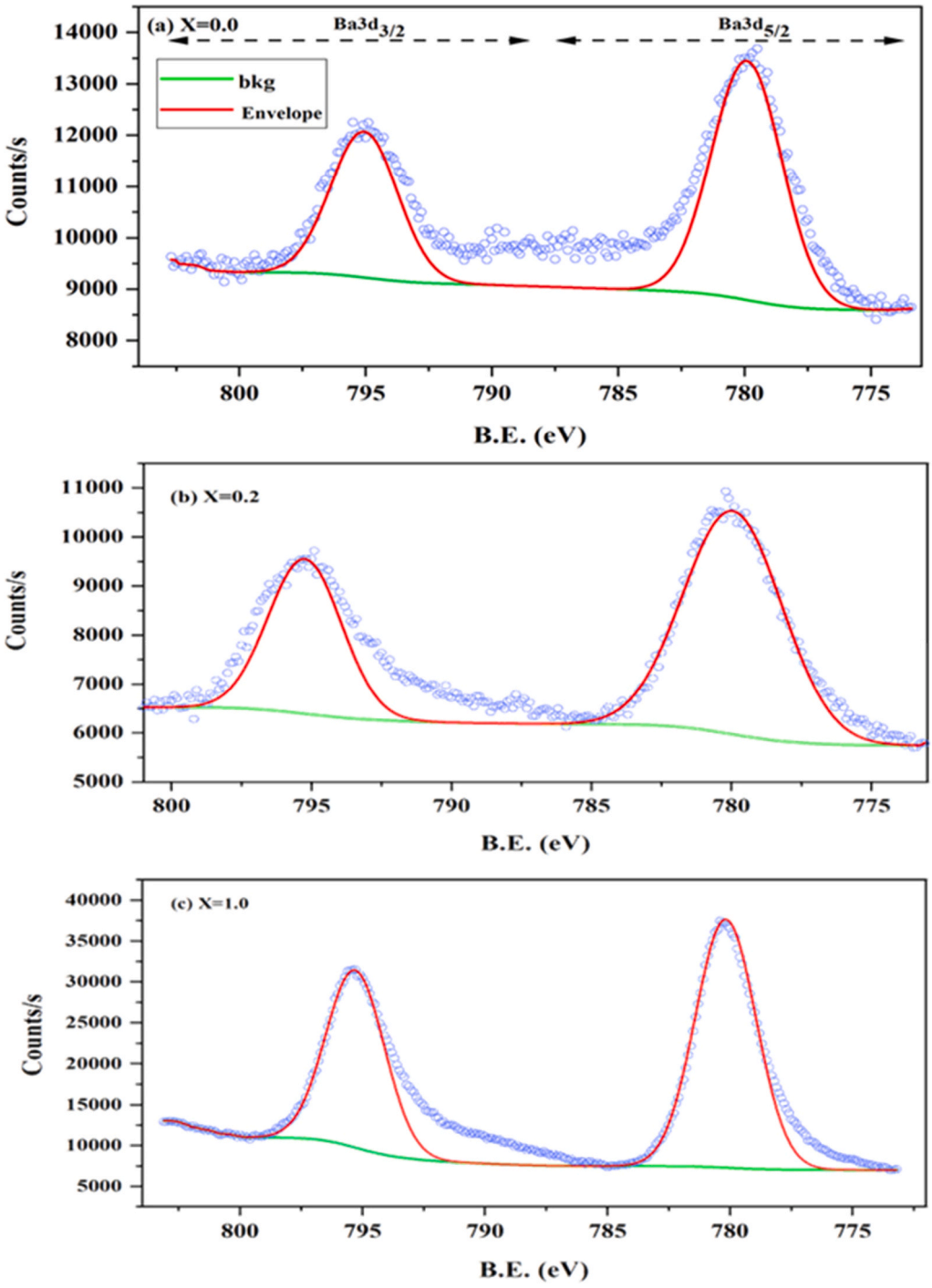

Fig. 11. Deconvoluted XPS spectra of Ba-3d (a), Sr-3d (b), Fe-2p (c), Zr-3d (e) and O-1s (f) of (1-x)BSFO/(x)BZO, x = 0.0, 0.2 and 1.0.

samples and the lack of any foreign elements aligned with the XRD and Raman results, apart from a faint C 1s signal at 285.2 eV, which is attributed to surface carbon atoms. C 1s is a commonly observed artifact in XPS spectra linked to C–C or C–H bonds, which does not indicate chemically bonded carbon within the material [72]. The binding energies of all identified elements are calibrated using the adventitious C 1s peak at 285.2 eV as the reference point.

The high-resolution XPS (HRXPS) spectra for each element for (1-x) BSFO/BZO composite with x = 0.2, compared to those of BSFO and BZO, are analyzed by deconvoluting their core energy levels using the Fit-yk software, as demonstrated in Fig. 11(a–e). Fig. 11a illustrates the HRXPS analysis of the Ba 3d peaks, where the Ba 3d signal is split into Ba $3d_{5/2}$ and Ba $3d_{3/2}$. These peaks are observed at binding energies of 780 eV and 795.1 eV, respectively, confirming that barium exhibits an oxidation state of +2 [73]. The same two peaks are detected in the 20% BSFO/BZO composite, although the Ba $3d_{3/2}$ peaks exhibit a shift toward higher binding energy by approximately 0.2 eV, likely attributed to ion interactions taking place during the co-precipitation synthesis process. Similarly, the XPS spectra of Sr 3d for the pure BSFO phase and nanocomposite with x = 0.2, as illustrated in Fig. 11b, exhibit two distinct peaks for each sample. The first peak is observed at approximately 135.2 eV, which is related to the Sr−$3d_{5/2}$ [74]. While the other

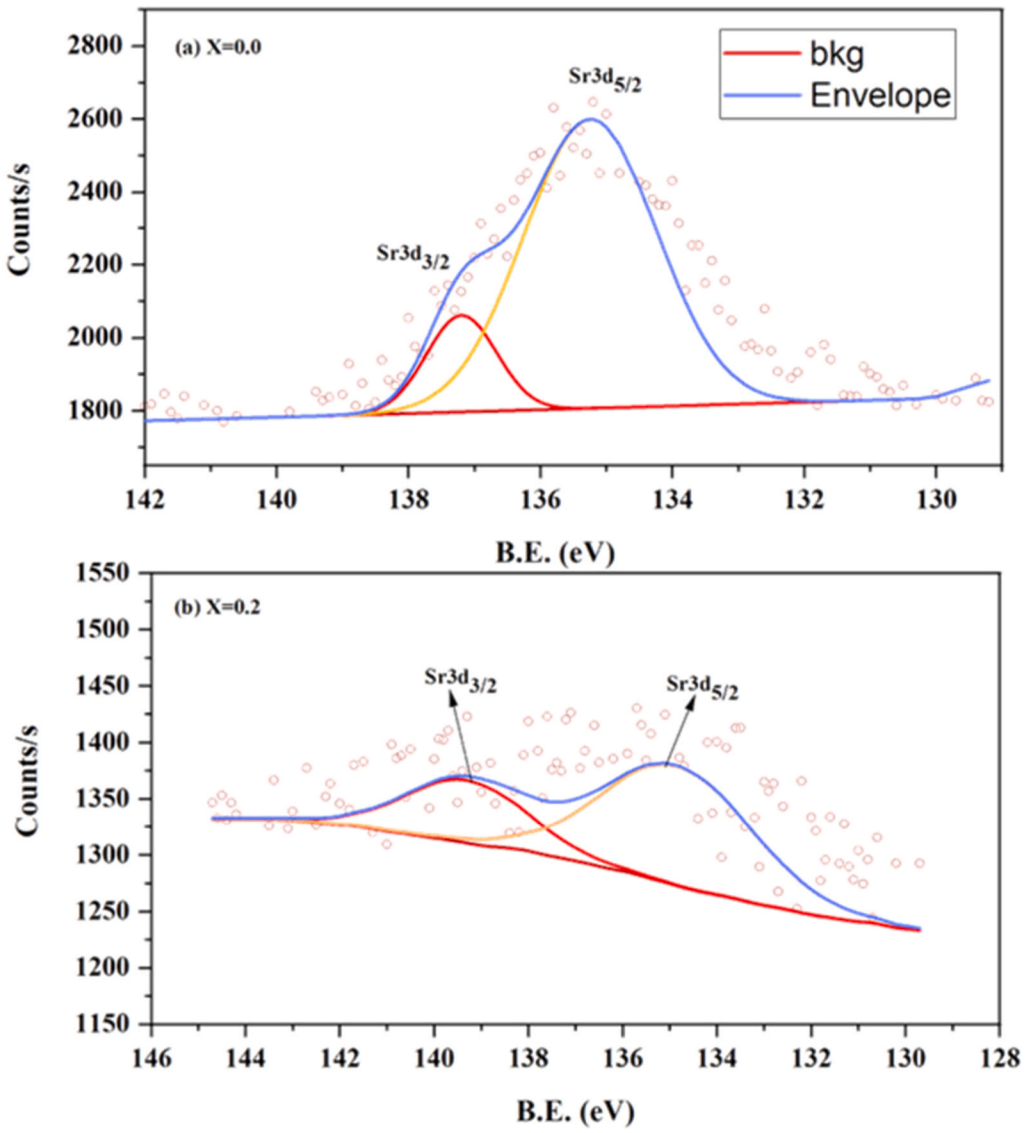

Fig. 11. (*continued*).

peak appeared at approximately 137.2 eV that related to Sr $3d_{3/2}$, with a slight positive shift compared to the reported literature values (133–135 eV), and a shift of the Sr $3d_{3/2}$ peak from 137 eV to 139 eV in the composite, this indicates a decrease in electron density around the Sr atoms. This observation suggests interfacial charge transfer and a stronger interaction with the surrounding matrix, ultimately leading to an increase in the effective binding energy. This provides clear evidence of the presence of Sr^{2+} ions.

As displayed in Fig. 11c, the deconvolution of the Fe 2p spectral line across all samples reveals two distinct components, Fe-$2p_{3/2}$ and Fe-$2p_{1/2}$, which result from spin–orbit splitting. For BSFO phase, the Fe $2p_{3/2}$ spectrum is deconvoluted into two separate peaks with binding energies around 711.5 eV and 713.7 eV. Meanwhile, the Fe $2p_{1/2}$ spectrum reveals two well-defined peaks at approximately 724.6 eV and 727.7 eV [72]. This indicates the existence of two distinct types of Fe ion bonds, corresponding to two different lattice sites for Fe ion incorporation: tetrahedral sites, which are associated with higher binding energies (713.7 eV and 727.7 eV), and octahedral sites, linked to lower binding energies (711.5 eV and 724.6 eV). Additionally, faint satellite peaks can be noted at 719.1 eV and 733.9 eV. These peaks are attributed to electronic transitions arising from charge transfer processes between Fe ions during the formation of ferrite [72]. The composite sample 20% SBFO/BZO shows the same six distinctive peaks as those listed above. But the binding energy of Fe $2p_{3/2}$ and Fe $2p1/_2$ moves marginally towards reduced values (710.7 eV and 723.7 eV, respectively). This indicates a higher electron density surrounding Fe, implying a partial reduction of Fe^{3+} to Fe^{2+} [75]. Zirconium was present in the form of Zr^{4+} cations in both the pristine BaZrO3 and 20% BSFO/BZO composite. This was confirmed by the Zr 3d spectra, which exhibited two distinct peaks at binding energies of 179 eV ($3d_{5/2}$) and 181.4 eV ($3d_{3/2}$) [76], without any observable shift, as shown in Fig. 11d. The ΔBE value is approximately 2.4 eV, indicating the oxidation state of Zr^{4+} [77]. The peak around 175.4 eV detected in the pure $BaZrO_3$ sample is linked to reduced zirconium species, which are related to oxygen-deficient regions or sub-oxide formation. In the composite, this feature is no longer observed, signifying the complete oxidation and stabilization of zirconium in the +4 state as a result of its interaction with other components.

As shown in Fig. 11e, the O 1s spectrum was deconvoluted into two distinct peaks at approximately 531.6 eV and 534 eV, corresponding to M-O lattice and the C-OH bonds of adsorbed water molecules, respectively [78].

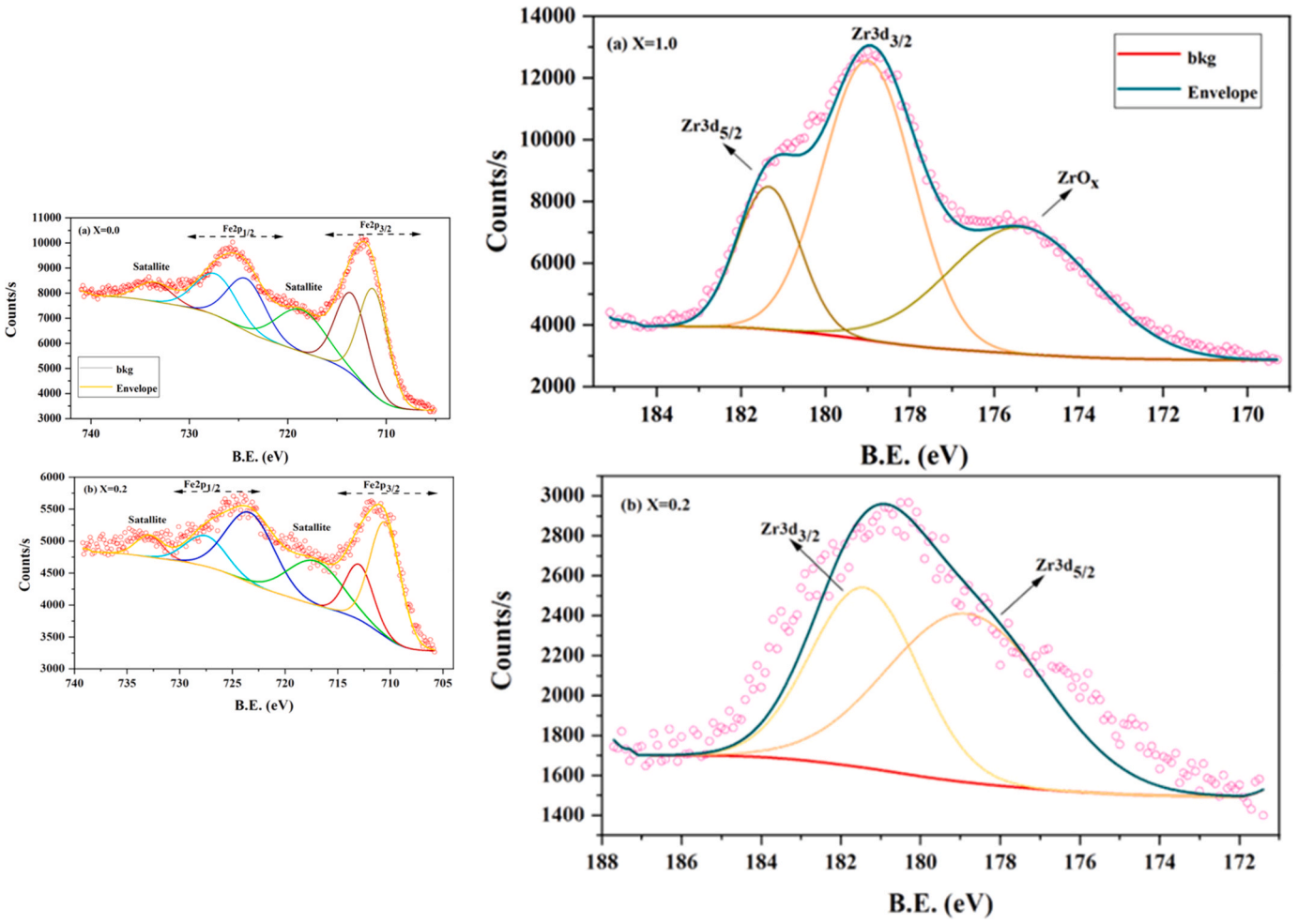

Fig. 11. (*continued*).

3.7. VSM analysis

Figs. 12(a) and 12(b) show the magnetic hysteresis (M–H) loop measurements at room temperature of the parent phases BSFO and BZO, respectively. The BSFO material exhibits a wide magnetic hysteresis loop with high saturation magnetization (M_s) of 57.95 emu/g, an intrinsic coercivity (H_c) of 3604.75 Oe, and a remanent magnetization (M_r) of 29.5 emu/g, affirming that the material exhibited the properties of a hard magnetic material [79]. These values are in good agreement with previously reported values for $Ba_{0.5}Sr_{0.5}Fe_{12}O_{19}$ [80,81]. Moreover, BSFO nanoparticles with a crystallite size of 43.9 nm, studied by Vizhi et al. [82], presented a higher saturation magnetization (64.4 emu/g) and coercivity (4.9 kOe) compared to those found in this work. This reduction in magnetic properties can be explained in terms of the differences in crystallite size and the presence of antiferromagnetic impurities of Fe_2O_3.

Conversely, BZO is non-magnetic with typical diamagnetic behavior, which arises due to its cubic perovskite structure with non-magnetic Ba^{2+} as well as non-magnetic Zr^{4+} ions [25,29]. As depicted in Fig. 12 (b), the M-H loop remains solely in the negative magnetization with negligible negative remnant magnetization ($M_r = 7.1 \times 10^{-3}$ emu/g) and zero coercivity. It reflects that no substantial paramagnetic or ferromagnetic contribution could surpass the diamagnetic background, even under high applied magnetic fields. It is worth mentioning that the presence of ZrO_2 as an impurity phase does not influence the magnetic properties of $BaZrO_3$, as ZrO_2 is a nonmagnetic oxide and is generally reported to be a diamagnetic material [83,84]. The minor observable hysteresis and negative M_r are probably artifacts arising from external factors, such as oxygen vacancies and defect complexes at grain boundaries. These imperfections can generate localized electronic states that exhibit slight polarization in a magnetic field, resulting in minor hysteresis characteristics or variations from perfect linear diamagnetism [85]. Interestingly, the M-H curves for the composite samples show a distinct kink, indicating that magnetic reversal in composite samples, particularly in composites with higher BZO content, occurs in a two-step process within the hard phase [38].

Magnetic properties of hexaferrites are strongly influenced by cation site occupancy, which governs their net magnetization [86]. Hexaferrite materials possess several crystallographic sites, tetrahedral, octahedral, and bipyramidal, that are preferentially occupied by Fe^{3+} magnetic ions. Akhtar et al. [87] reported that Fe ions are typically distributed among two tetrahedral sites, nine octahedral sites, and one trigonal site. The magnetic moments associated with these sites are coupled via super-exchange interactions and align either parallel or antiparallel to one another.

From M-H curves, the main magnetic parameters such as saturation magnetization (M_s) and remanent magnetization (M_r) are extracted and are listed in Table 6. It can be seen that the saturation magnetization significantly decreases from 57.95 emu/g for BSFO to 12.77 emu/g for the BSFO/BZO nanocomposite with x = 0.8. A similar trend is noticed in the remanent magnetization, which decreases with increasing content of BZO. The reduction in magnetization can be attributed to the redistribution of magnetic interactions among the Fe sublattices in the composite samples, as explained in the Raman analysis section. The decrease in the Raman band areas at 332 and 408 cm^{-1} indicates weakening of the FeO_6 octahedral vibrations at the 12k sites, reducing the

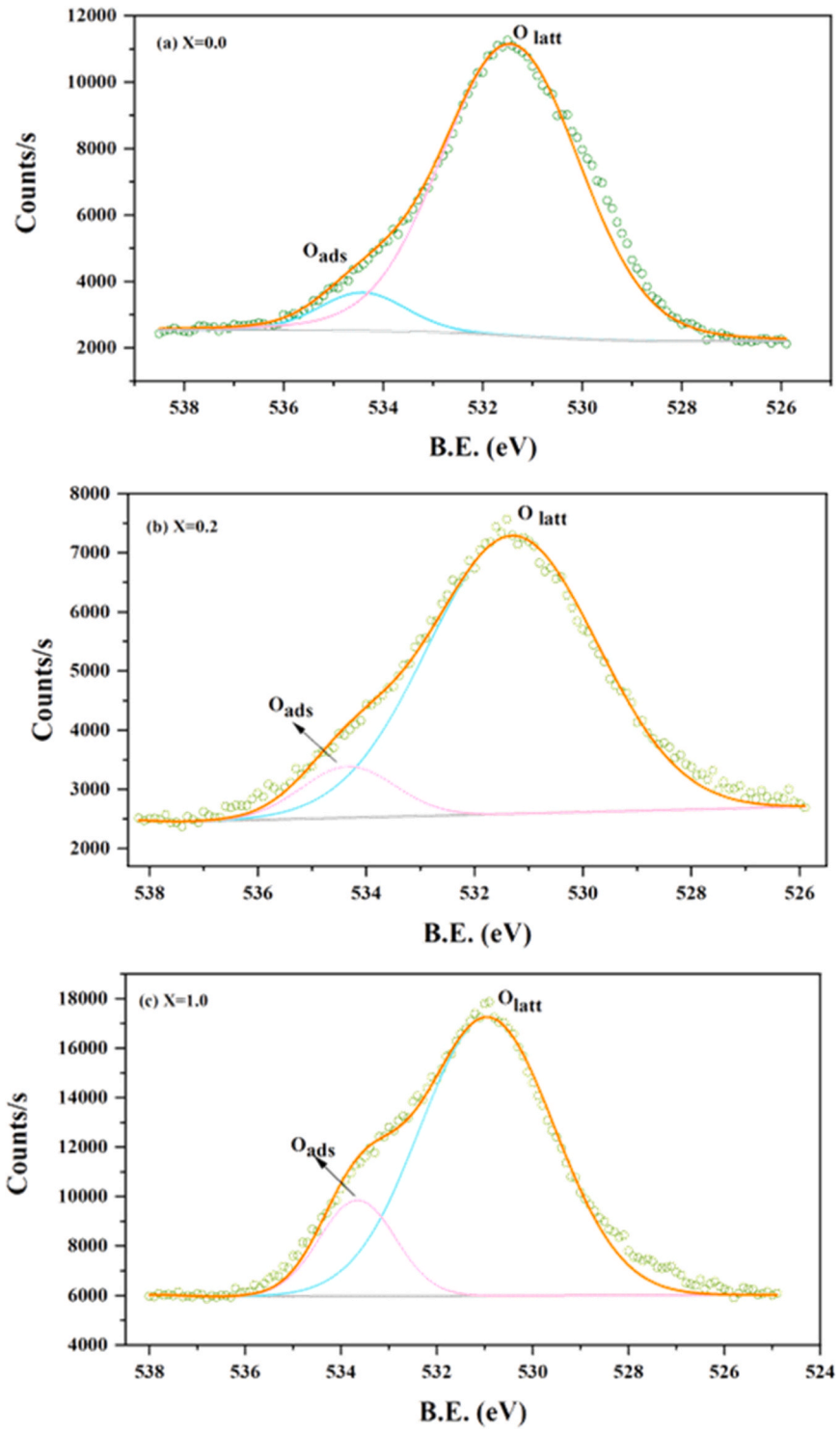

Fig. 11. (*continued*).

contribution of the spin-up sublattice and weakening the associated superexchange interactions. In contrast, the increased areas of the bands at 612 and 682 cm^{-1} suggest stronger Fe–O stretching vibrations at the octahedral ($4f_2$) and tetrahedral ($4f_1$) sites, which are linked to spin-down sublattices. This enhances magnetic compensation between anti-parallel sublattices, resulting in reduced ferrimagnetic ordering and consequently lower net magnetization. The impact is additionally heightened by the reduced magnetic phase fraction of the magnetic phase per unit mass and the presence of diamagnetic BZO and ZrO_2, which dilute the overall magnetic response [25]. The magnetization values, normalized to the unit mass of BSFO, are presented in Table 6. As shown, the overall reduction in magnetization with increasing BZO content is mainly caused by the dilution of the magnetic BSFO phase. However, when the values are normalized to the BSFO fraction, the saturation magnetization shows only minor changes, which can be attributed to slight structural distortions at the interfaces and variations in grain size.

The coercivity of BSFO decreases from 3604 Oe to 3555.87 Oe for the nanocomposite with x = 0.10, after which it increases unexpectedly, reaching a maximum value of 3935.79 Oe for x = 0.20. With further

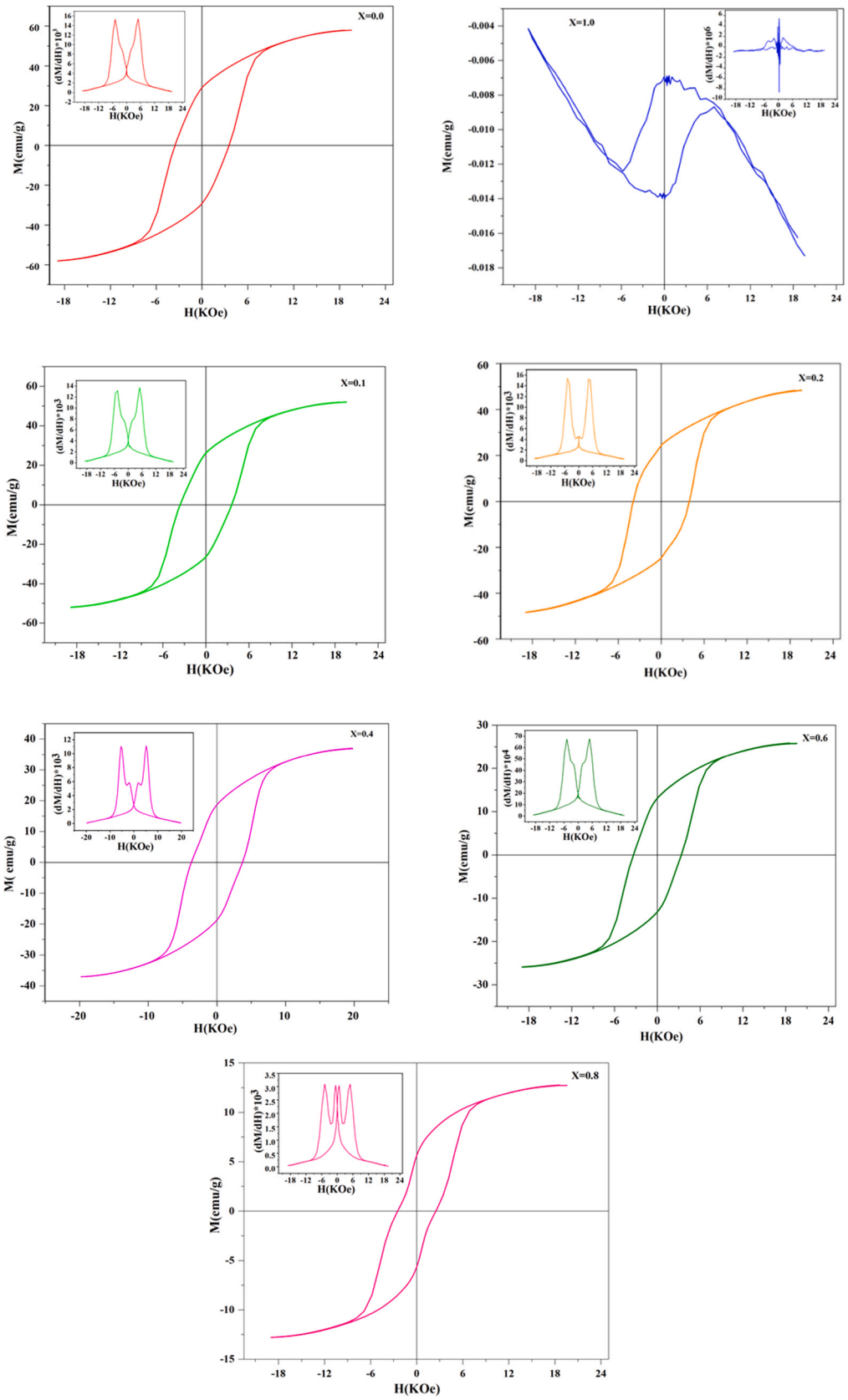

Fig. 12. M - H hysteresis loops of BSFO and BZO nanoparticles and (1-x)BSFO/(x)BZO nanocomposites. The inset shows dM/dH Versus H for all samples.

Table 6
magnetic parameters determined from VSM experimental and fitted data using the law of approach to saturation (LAS) models for (1-x)$Ba_{0.5}Sr_{0.5}Fe_{12}O_{19}$/(x)$BaZrO_3$ nanocomposites.

Magnetic parameters	x = 0.0	x = 0.1	x = 0.2	x = 0.4	x = 0.6	x = 0.8
experimental (M-H) curve						
M_s (emu/g)	57.95	52.21	48.53	37.04	25.86	12.77
M_s^{BSFO}	57.95	85.01	60.66	61.73	64.65	63.85
H_c(Oe)	3604.75	3555.87	3935.79	3715.84	3270.93	2606.08
M_r (emu/g)	29.09	26.21	24.51	18.62	13.03	5.59
M_r /M_s	0.502	0.502	0.505	0.503	0.504	0.437
$M = M_s \times \left[1 - \frac{\beta}{H^2}\right]$						
M_s(emu/g)	58.84	52.80	48.70	37.55	26.23	12.92
$\beta \times 10^7$ (Oe)^2	1.13	1.12	1.24	1.16	1.04	0.91
$K_{eff} \times 10^5$(erg/g)	3.82	3.42	3.33	2.48	1.64	0.75
$H_a \times 10^4$(Oe)	1.30	1.29	1.37	1.32	1.25	1.17
$n_B(\mu_B)$	11.45	9.51	8.06	5.13	2.82	1.01
N	93.04	105.05	112.44	145.61	216.93	478.37
R^2	0.951	0.951	0.926	0.959	0.958	0.955
$M = M_s\left[1 - \frac{1}{15}\frac{H_a^2}{H^{1/2}(H^{3/2} + H_R^{3/2})}\right] + \chi H$						
M_s(emu/g)	60.00	54.50	49.80	38.90	27.06	13.03
$H_a \times 10^4$(Oe)	1.52	1.54	1.54	1.57	1.48	1.30
$H_R \times 10^{-6}$ (Oe)^2	2.00	2.17	2.50	2.19	2.20	0.80
χ	0.0016	0.0014	0.0013	0.0012	0.0009	0.0005
R^2	0.982	0.973	0.993	0.942	0.934	0.967

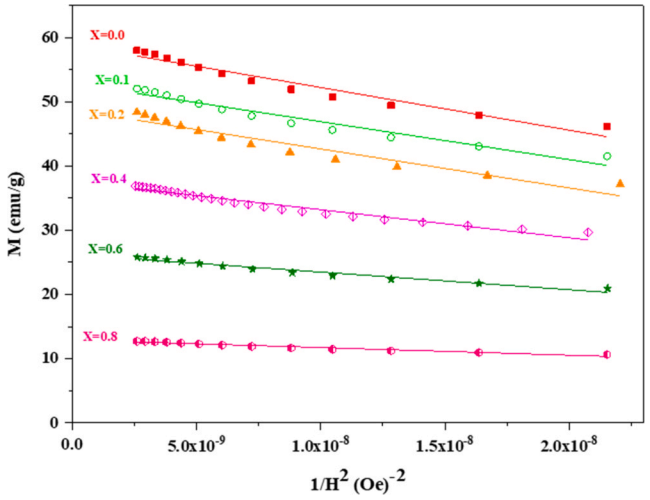

Fig. 13. M versus 1/H^{2}plots for BSFO nanoparticles and (1-x)BSFO/(x)BZO nanocomposites.

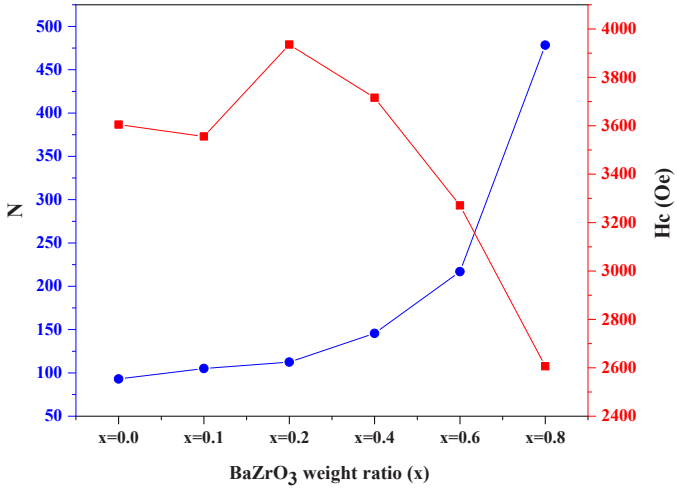

Fig. 14. The variation in coercivity (H_c) with demagnetization field (N).

increase in x, the coercivity decreases again, reaching 2606.08 Oe for the nanocomposite with x = 0.80. The non-monotonic variation in coercivity with BZO content may arise from changes in particle size within the composite samples [88]. The coercivity (H_c) is strongly affected by several factors, including the magnetic anisotropy constant, material defects, grain boundaries, and grain size [89]. The highest coercivity (H_c) observed for the nanocomposite with x = 0.2 is mainly due to its smaller grain size and larger surface area. When grains get smaller, the number of grain boundaries increases, which makes it harder for magnetic domain walls to move and therefore requires a stronger external magnetic field to shift them [90]. Moreover, the larger surface area and enhanced interfacial disorder led to localized changes in exchange coupling and magnetic anisotropy. This makes it even harder for the domain walls to move, thereby increasing the coercivity.

The squareness ratio indicates how effectively the applied magnetic field H aligns with the easy magnetization axis M. For materials with uniaxial anisotropy, the expected numerical values of the squareness ratio (M_r /M_s) are typically 0.5 [91]. The obtained M_r /M_s ratios are listed in Table 6. For all samples, the squareness ratio values are very close to 0.5, characteristic of random orientations of the magnetic domains [92]. This behavior suggests a multidomain magnetic arrangement in the prepared samples, aligning with the TEM findings.

The interphase exchange coupling between the soft and hard magnetic phases is evaluated using the switching field distribution (SFD), which is obtained from the first derivative of the magnetization curve (dM/dH as a function of H). As shown in the inset of Fig. 12 for BSFO, the SFD exhibits two extinguished peaks symmetrically positioned about H = 0, with a minimum at the center. This behavior is characteristic of hard magnetic materials [38], in which strong magnetic anisotropy stabilizes the magnetization against small applied fields. The symmetric nature of these peaks stems from the inherent hysteresis characteristics of the material. As regards the BZO sample, the small deviation from ideal linear diamagnetic behavior is likely caused by intrinsic defects or trace impurities that locally disrupt the crystal symmetry, thereby allowing magnetic moments to form. Additionally, the presence of a small amount of ZrO_2 can induce microstrain in the $BaZrO_3$ matrix due to lattice mismatch. This strain may further enhance the formation of

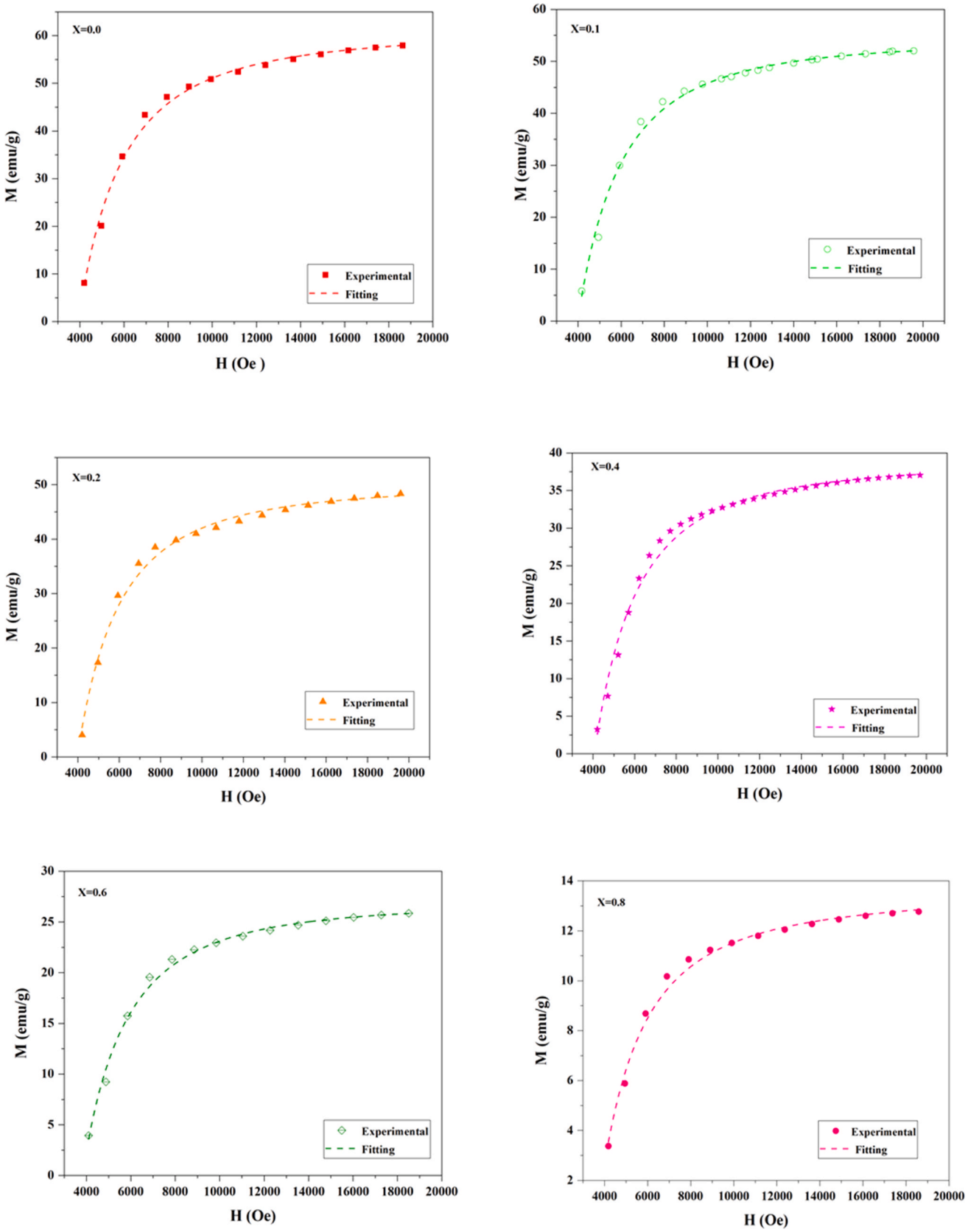

Fig. 15. Experimental data fitted using the law of approach to saturation (LAS).

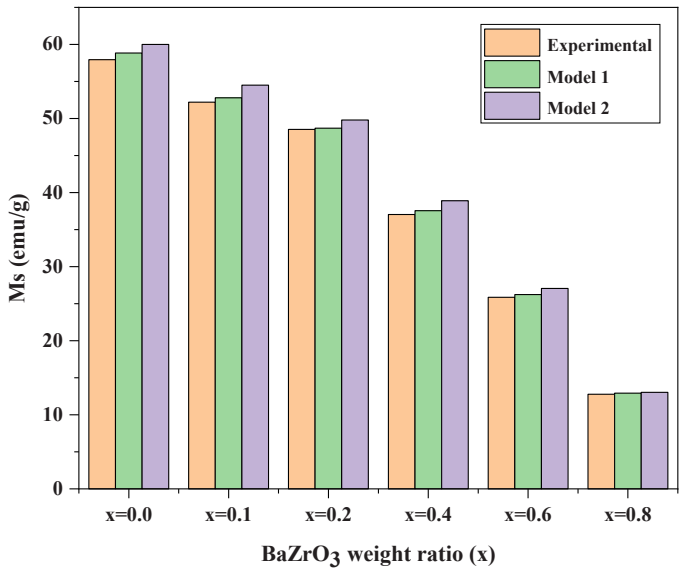

Fig. 16. The difference between the experimental saturation magnetization and that obtained from the law of approach to saturation model.

oxygen vacancies in the affected regions. In perovskite oxides, oxygen vacancies are well known to play a key role in magnetic anomalies [93,94], as they can trap electrons and form F centers, which behave as localized magnetic moments. The correlation between the extrinsic oxygen vacancies induced by the high calcination temperature and the origin of magnetism in non-magnetic materials has been previously examined [39,94]. The dM/dH curves for nanocomposites are governed primarily by the magnetic response of the $Ba_{0.5}Sr_{0.5}Fe_{12}O_{19}$ phase, with modifications arising from microstructural and interfacial effects introduced by the nonmagnetic $BaZrO_3$ phase. The prominent peaks observed at higher magnetic fields correspond to BSFO. A noticeable weak shoulder appears in the vicinity of zero magnetic field related to domain wall pinning processes within $Ba_{0.5}Sr_{0.5}Fe_{12}O_{19}$ grains, as well as to magnetically disordered regions formed at $Ba_{0.5}Sr_{0.5}Fe_{12}O_{19}$ / $BaZrO_3$ interfaces. The introduction of the diamagnetic phase can induce strain, defects, and surface spin disorder in the hard ferrite, thereby creating regions with reduced anisotropy that respond at lower applied fields. This behavior is consistent with an apparent negative remanent magnetization at low field for $BaZrO_3$. The increasing $BaZrO_3$ concentration leads to a noticeable peak near zero field, indicating a change in the magnetization reversal mechanism. This is likely due to BZO acting as an insulating barrier that suppresses the exchange coupling among BSFO particles. In contrast, the presence of a single peak at elevated fields in the nanocomposite with x = 0.2 indicates its significant magnetic anisotropy, consistent with its highest coercivity value.

To examine the dependence of magnetization on the applied magnetic field in the high-field region, two models of the saturation approach law are applied. The first model is a simplified expression used to describe the approach to saturation straightforwardly [95].

$$M = M_s \times \left[1 - \frac{\beta}{H^2}\right] \tag{7}$$

According to Eq. (7), the magnetization (M) plotted against $1/H^2$ yields straight lines, as depicted in Fig. 13. The corresponding fitting parameters are summarized in Table 6. The point of intersection of the linear fit with the magnetization axis represents the value of M_s, whereas the slope (M_s β) indicates the value of the constant β.

As shown in Table 6, a significant reduction in the saturation magnetization is observed when the $BaZrO_3$ ratio rises. The estimated M_s values are close to the experimental values, estimated from (M-H) curves. The reduction rate in M_s is 78.55% for the nanocomposite with x = 0.8, which is consistent with the amount of $BaZrO_3$ and reflects the dilution of the magnetic phase as well as the disruption of magnetic exchange interactions among BSFO grains caused by the non-magnetic $BaZrO_3$ matrix.

Relying on the computed values of $M_s$and β, the effective magnetic anisotropy coefficient (K_{eff}) is established utilizing the subsequent relationship [95]:

$$K_{eff} = M_s\sqrt{\frac{15\quad\beta}{4}} \tag{8}$$

The magnetic moment (n_B) of the nanocomposites, expressed in Bohr magnetons per unit formula, can be estimated from experimental data using the following relation.

$$n_B = \frac{M_w M_s}{5585} \tag{9}$$

where M_w is the molecular weight of the composite and 5585 represents the magnetic factor.

As observed in Table 6, as the content of the nonmagnetic phase BZO increases relative to the hard BSFO phase, K_{eff} and n_B values decrease. This reduction is mainly due to the partial reduction of Fe^{3+} ($5\mu_B$) to Fe^{2+} ($4\mu_B$), as discussed in the XPS section. The resulting Fe^{2+} weakens the Fe–O–Fe superexchange interactions by introducing Fe^{2+}–O– Fe^{3+}, reducing orbital overlap and increasing spin disorder, especially at defect-rich interfaces. Consequently, the saturation magnetization and overall magnetic ordering decrease due to the lower magnetic moment of Fe^{2+} and the formation of magnetically disordered interfacial regions. In addition, structural defects such as oxygen vacancies and lattice strain, suggested by changes in the Raman spectra, can distort the local Fe–O–Fe bond angles. This weakens the magnetic exchange interactions and can affect both spin canting and magnetic anisotropy.

The anisotropy field (H_a) can be determined using the following equation:

$$H_a = \frac{2K_{eff}}{M_s} \tag{10}$$

Change in anisotropy field (H_a) shows the same behavior as changes in H_c, and can help explain the observed changes in H_c. The shift in the coercive field is likely due to changes in the overall magnetocrystalline anisotropy energy, which are linked to magnetoelectric (ME) coupling. These effects arise from the compressive stress on the BSFO phase, caused by lattice mismatch between the BSFO and BZO phases [96]. As the anisotropy field decreases, the energy barriers become lower, allowing domain walls to move more easily and ultimately leading to reduced coercivity in the composites, and the opposite effect occurs when the anisotropy field increases [97].

The demagnetizing field N can be estimated using the calculated values of H_c, M_s and K_{eff} as follows [38]:

$$H_c = 0.48\left[\frac{2K_{eff}}{\mu_0 M_s} - NM_s\right] \tag{11}$$

where μ_0 is vacuum permeability.

The demagnetizing field N increases as the $BaZrO_3$ weight ratio rises; however, the nanocomposite with x = 0.2 exhibits a comparatively lower demagnetization value. As depicted in Fig. 14, the change in N is found to vary inversely in relation to H_c. Nanocomposite with 0.2, which exhibits greater coercivity and demonstrates increased resistance to demagnetization.

The second model (Eq. (12)) provides a more accurate description of the magnetization behavior in the high-field region, where the magnetization increases only slightly with further increase in the applied magnetic field. In this regime, the magnetization process is dominated by the reversible rotation of magnetic moments within domains rather than domain wall motion [95].

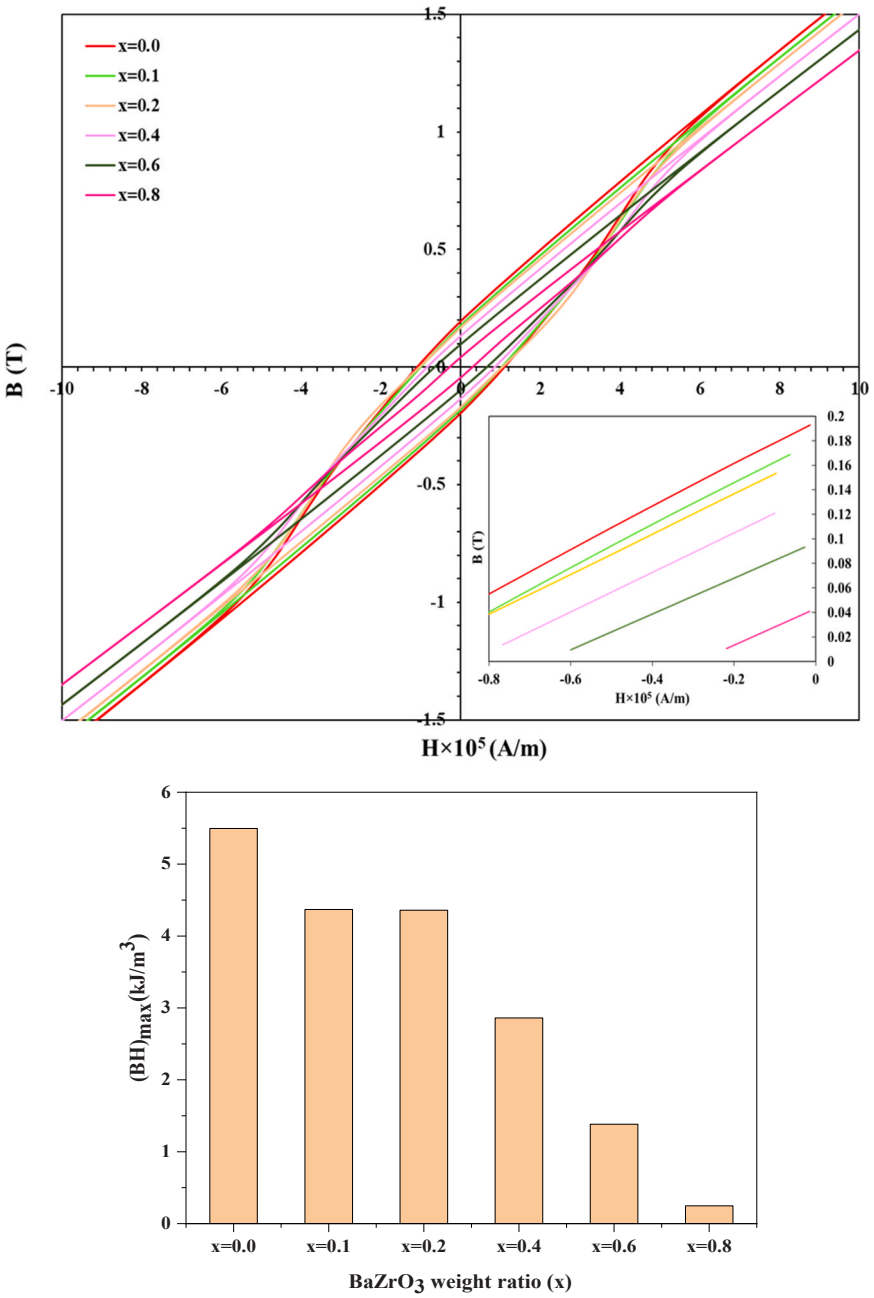

Fig. 17. a: (B-H) curves with an inset highlighting the second-quadrant demagnetization behavior. b: The variation of $(BH)_{max}$ with BZO weight ratio.

$$M = M_s\left[1 - \frac{1}{15}\frac{H_a^2}{H^{1/2}(H^{3/2} + H_R^{3/2})}\right] + \chi H \tag{12}$$

Where M_s represents the saturation magnetization, H_a denotes the local magnetic anisotropy field, H_R signifies the exchange field, and χH refers to the high-field paramagnetic susceptibility which has been suggested to originate from defects within ferromagnetic materials.

Fig. 15 (a–e) illustrate a typical fit for the prepared samples using Eq. (12), with the associated parameters outlined in Table 4. As shown in Fig. 16, the M_s values estimated by model 1 are closer to the experimental M_s than those from model 2. However, both models still fit the data well, as indicated by the high R^2 values of the fitted curves. As shown in Table 6, the variation of H_R shows the same behavior as changes in H_c. The reduction in H_R observed in composites with a higher BZO weight ratio can be attributed to weaker exchange interactions between BSFO grains [98]. As a result, a lower external magnetic field is required to overcome local spin disorder at high field strengths. Additionally, increasing the diamagnetic BZO weight ratio leads to a decrease in χ, confirming the progressive dilution of the material's ferromagnetic character.

The maximum energy product $(BH)_{max}$ indicates the maximum magnetic energy a magnet can store per unit volume and is typically used as an indicator of magnet strength. In this study, the highest obtainable energy product of the synthesized samples is assessed by transforming the magnetic hysteresis (M–H) loops into magnetic induction (B–H) loops as a function of the applied magnetic field, as illustrated in Fig. 17a. Typically, $(BH)_{max}$ is obtained from the demagnetization curve (second quadrant) of the hysteresis loop, as shown in the inset of Fig. 17a. The variation of $(BH)_{max}$ with the weight ratio x is illustrated in Fig. 17b. The variation in $(BH)_{max}$ follows the same trend as the remanent magnetization (M_r) and saturation magnetization (M_s) with increasing BZO content. BSFO, with a maximum energy product of

5.49 kJ/m^3 at room temperature, confirms its suitability for low-cost industrial applications such as motors and magnetic separators. Ferrites have advantages over rare-earth magnets in terms of chemical stability, strong corrosion resistance, and high thermal stability, but their magnetic strength is significantly lower. On the other hand, NdFeB magnets have the highest magnetic energy density (~200–400 kJ/m^3) and are very important for high-performance applications. However, they have significant drawbacks, including temperature sensitivity, high cost, rare-earth reliance, and demagnetization risk [99]. The decline in $(BH)_{max}$ with increasing BZO content is linked to the associated drop in M_s and M_r. Furthermore, the $(BH)_{max}$ value of the parent BSFO phase is higher than that of BFO (3.5 kJ/m^3) but lower than that of SFO (13.68 kJ/m^3) [8]. Based on the results discussed above, we conclude that the 0.8BSFO/0.2BZO nanocomposite exhibits the highest coercivity, and its $(BH)_{max}$ remains sufficiently high for use in permanent magnets, motors, and generators. In contrast, composites with a higher BZO weight fraction are more suitable for electromagnetic interface, EMI suppression, including EMI filters, cable shielding, and microwave absorption.

4. Conclusions

To better understand how the structure affects the magnetic behavior of the (1-x)BSFO/(x)BZO nanocomposites, several characterization techniques were used. XRD analysis of these nanocomposites showed distinct peaks for each phase, and the phase volume fraction and microstructure were further confirmed through Rietveld refinement. Among the BSFO nanocomposites, the nanocomposite with $x = 0.2$ exhibited the smallest crystallite size of 36.5 ± 0.47 nm, compared with 53.6 ± 0.54 nm for parent BSFO. Minor changes in lattice parameters cause a slight distortion of the crystal lattice, reflected in a reduced c/a ratio from 3.943 to 3.917. Moreover, BET measurements indicated that the 20% BSFO/BZO composite had a greater surface area (0.91 m^2/g) and a smaller average pore size of 2.80 nm. TEM observations showed that increasing the BZO content promoted clustering and stacking of BZO particles with the hexaferrite particles. This reduced interface uniformity and likely weakened the exchange coupling between hexaferrite grains. HRTEM images revealed two separate lattice fringes at the interface, separated by a firmly bonded boundary, suggesting no chemical interaction between them. FTIR measurements showed a shift of the Fe–O stretching modes from 594.28 cm^{-1} in BSFO to 562.29 cm^{-1} for $x = 0.8$, consistent with corresponding changes in the lattice parameter. Debye temperature (Θ_D) estimated from phonon modes indicated values of 744.69 K for BSFO and 800.20 K for BZO. As the BZO content increased, the Debye temperature rose, reaching 815.75 K and 808.57 K for $x = 0.6$ and 0.8, respectively, reflecting the increasing influence of BZO's stiffer perovskite structure. Raman spectroscopy indicated that the observed broad Raman peaks are due to defects within the BZO phase. The peak area analysis showed Fe-ion redistribution among different crystal sites, likely affecting the composite's magnetization. XPS analysis confirmed the expected oxidation states of the elements and showed that some Fe^{3+} ions were reduced to Fe^{2+}. This partial reduction is likely an important factor contributing to changes in the overall magnetization of the nanocomposites. Magnetic measurements showed a significant decrease in the saturation magnetization (M_s) from 57.95 g^{-1} to 12.77 g^{-1} as the BZO weight ratio increased to 0.8. Similarly, the remanent magnetization (M_r) and maximum energy product $(BH)_{max}$ decreased from 29.09 g^{-1} and 5.496 m^{-3} to 5.59 g^{-1} and 0.247 m^{-3}, respectively. This behavior can be primarily attributed to magnetic dilution and changes in the material's structure. The coercivity (H_c) of the BSFO material reduced from 3604 Oe to 3555.87 Oe for the nanocomposite with $x = 0.10$. However, the composite with $x = 0.20$ had a higher coercivity of 3935.79 Oe. The increase in coercivity can be attributed to several factors, including smaller grain size, greater surface area, and interfacial disorder, all of which limit domain wall movement within grains and consequently enhance magnetic anisotropy.

CRediT authorship contribution statement

Bakeer D. El-Saied: Writing – review & editing, Investigation, Formal analysis, Data curation, Conceptualization. **E.M. El-Maghraby:** Writing – review & editing, Validation, Project administration, Conceptualization. **R. Awad:** Writing – review & editing, Conceptualization. **Shaimaa A. Habib:** Writing – review & editing, Validation, Data curation. **Kh. Elaskary:** Writing – original draft, Methodology, Investigation, Formal analysis, Data curation.

Funding

No funding.

Declaration of Competing Interest

The authors declare that they have no known competing financial interests or personal relationships that could have appeared to influence the work reported in this paper.

Acknowledgement

The authors express their sincere appreciation to the Solid State Laboratory, Department of Physics, Faculty of Science, Damanhour University, for facilitating the preparation of the experimental samples.

Data availability

The data that support the findings of this study are available from the corresponding author upon reasonable request.

References

[1] B. Ates, S. Koytepe, A. Ulu, C. Gurses, V.K. Thakur, Chemistry, structures, and advanced applications of nanocomposites from biorenewable resources, Chem. Rev. 120 (2020) 9304–9362, https://doi.org/10.1021/acs.chemrev.9b00553.
[2] O.D. Dastjerdi, H. Shokrollahi, S. Mirshekari, A review of synthesis, characterization, and magnetic properties of soft spinel ferrites, Inorg. Chem. Commun. 153 (2023) 110797, https://doi.org/10.1016/j.inoche.2023.110797.
[3] T. Dippong, O. Cadar, I.G. Deac, L.B. Tudoran, E.A. Levei, Influence of Ni2+ substitution by Co^{2+} on the morphology and magnetic properties of single domain $Co_\alpha Ni_{0.9-\alpha}Zn_{0.1}Fe_2O_4$ nanoparticles, J. Alloy. Compd. 952 (2023) 170074, https://doi.org/10.1016/j.jallcom.2023.170074.
[4] T. Dippong, R.A. Mereu, Effect of La 3+ on thermal, structural and morphological properties of Zn–Co ferrite spinel-based pigments, Ceram. Int. 50 (2024) 10314–10324, https://doi.org/10.1016/j.ceramint.2023.12.343.
[5] B. Abraime, K. El Maalam, L. Fkhar, A. Mahmoud, F. Boschini, M.A. Tamerd, A. Benyoussef, M. Hamedoun, E.K. Hlil, M. Ait Ali, A. El Kenz, O. Mounkachi, Influence of synthesis methods with low annealing temperature on the structural and magnetic properties of CoFe2O4 nanopowders for permanent magnet application, J. Magn. Magn. Mater. 500 (2020) 166416, https://doi.org/10.1016/j.jmmm.2020.166416.
[6] S.K. Godara, M. Singh, V. Kaur, S.B. Narang, A.K. Sood, Effect of calcium solubility on structural, microstructural and magnetic properties of M-type barium hexaferrite, Ceram. Int. 47 (2021) 20399–20406, https://doi.org/10.1016/j.ceramint.2021.04.048.
[7] C.J. Fernández, C. Sangregorio, J. de la Figuera, B. Belec, D. Makovec, A. Quesada, Progress and prospects of hard hexaferrites for permanent magnet applications, J. Phys. Appl. Phys. 54 (2021) 153001, https://doi.org/10.1088/1361-6463/abd272.
[8] S.K. Moatoshi, S.D. Sah, J.P. Kaushik, Borah, Structural and magnetic properties of M-type hexaferrite nanoparticles: a comparative analysis of BaFe12O19 and SrFe12O19 synthesized via chemical co-precipitation, Ceram. Int. 50 (2024) 22599–22607, https://doi.org/10.1016/j.ceramint.2024.03.361.
[9] A. Ali, H. Zafar, M. Zia, I. ul Haq, A.R. Phull, J.S. Ali, A. Hussain, Synthesis, characterization, applications, and challenges of iron oxide nanoparticles, Nanotechnol. Sci. Appl. 9 (2016) 49–67, https://doi.org/10.2147/NSA.S99986.
[10] D.A. Vinnik, F.V. Podgornov, N.S. Zabeivorota, E.A. Trofimov, V.E. Zhivulin, A. S. Chernukha, M.V. Gavrilyak, S.A. Gudkova, D.A. Zherebtsov, A.V. Ryabov, S. V. Trukhanov, T.I. Zubar, L.V. Panina, S.V. Podgornaya, M.V. Zdorovets, A. V. Trukhanov, Effect of treatment conditions on structure and magnetodielectric properties of barium hexaferrites, J. Magn. Magn. Mater. 498 (2020) 166190, https://doi.org/10.1016/j.jmmm.2019.166190.
[11] X. Liu, W. Zhong, S. Yang, Z. Yu, B. Gu, Y. Du, Influences of La3+ substitution on the structure and magnetic properties of M-type strontium ferrites, J. Magn. Magn. Mater. 238 (2002) 207–214, https://doi.org/10.1016/S0304-8853(01)00914-3.

[12] A.M. Alsmadi, I. Bsoul, S.H. Mahmood, G. Alnawashi, K. Prokeš, K. Siemensmeyer, B. Klemke, H. Nakotte, Magnetic study of M-type doped barium hexaferrite nanocrystalline particles, J. Appl. Phys. 114 (2013) 243910, https://doi.org/10.1063/1.4858383.

[13] V. P. Singh, G. Kumar, P. Dhiman, R. K. Kotnala, J. Shah, K. M. Batoo, M. Singh, Structural, dielectric and magnetic properties of nanocrystalline BaFe12O19 hexaferrite processed via sol-gel technique, Adv. Mater. Lett. 5 (2014) 447–452, https://doi.org/10.5185/amlett.2014.554.

[14] S. Iqbal, G. Kotnala, J. Shah, S. Ahmad, Barium ferrite nanoparticles: a highly effective EMI shielding material, Mater. Res. Express 6 (2019) 5, https://doi.org/10.1088/2053-1591/ab02a4.

[15] N. Tran, M.Y. Lee, W.H. Jeong, T.L. Phan, N.Q. Tuan, B.W. Lee, Thickness independent microwave absorption performance of La-doped BaFe12O19 and polyaniline composites, J. Magn. Magn. Mater. 538 (2021) 168299, https://doi.org/10.1016/j.jmmm.2021.168299.

[16] R. Perez-Gonzalez, S. Cherepanov, A.I. Oliva, A. Zakhidov, A. Encinas, H. Flores-Zuñiga, S. Diaz-Castañon, J. Oliva, Highly efficient flexible CNT based supercapacitors fabricated with magnetic BaFe12O19 nanoparticles and biodegradable components, J. Phys. Chem. Solids 155 (2021) 110115, https://doi.org/10.1016/j.jpcs.2021.110115.

[17] Y. Marouani, J. Massoudi, M. Noumi, A. Benali, E. Dhahri, P. Sanguino, M.P. F. Graça, M.A. Valente, B.F.O. Costa, Electrical conductivity and dielectric properties of Sr doped M-type barium hexaferrite BaFe12O19, RSC Adv. 11 (2021) 1531–1542, https://doi.org/10.1039/D0RA09465J.

[18] B.F.O. Costa, A. Benali, B.J.C. Vieira, J.C. Waerenborgh, J. Pina, Y. Marouani, E. Dhahri, Mössbauer and optical investigations on Sr doped M-type BaFe12O19 hexaferrites produced via autocombustion, Crystals 15 (2025) 291, https://doi.org/10.3390/cryst15040291.

[19] Y. Marouani, A. Mabrouki, R. Dhahri, E. Dhahri, B.F.O. Costa, Experimental and theoretical studies of structural, magnetic and electronic properties of Ba1−xSrxFe12O19 (x = 0, 0.5, 1) hexaferrites, Inorg. Chem. Commun. 136 (2022) 109163, https://doi.org/10.1016/j.inoche.2021.109163.

[20] S. Hazra, B. Ghosh, M. Patra, R. Jani, S.R. Vadera, N.N. Ghosh, A novel 'one-pot' synthetic method for preparation of (Ni0.65Zn0.35Fe2O4)x–(BaFe12O19)1 − x nanocomposites and study of their microwave absorption and magnetic properties, Powder Technol. 279 (2015) 10–17, https://doi.org/10.1016/j.powtec.2015.03.046.

[21] S.M. Hoque, C. Srivastava, V. Kumar, N. Venkatesh, H.N. Das, D.K. Saha, K. Chattopadhyay, Exchange-spring mechanism of soft and hard ferrite nanocomposites, Mater. Res. Bull. 48 (2013) 2871–2877, https://doi.org/10.1016/j.materresbull.2013.04.009.

[22] I. Syed, S.A. Lima, N. Deb, M. Al-mamun, S.M. Hoque, Performance evaluation of dextran-coated CaFe12O19/MnFe2O4 exchange-spring composites for the self-heating properties at radio frequency field, Front. Chem. 12 (2024) 1347113, https://doi.org/10.3389/fchem.2024.1347113.

[23] L. Rifai, F. Fattouh, K. Habanjar, N. Yaacoub, R. Awad, Exchange spring behaviour in BaFe12O19/CoFe2O4 magnetic nanocomposites, J. Alloy. Compd. 868 (2021) 159072, https://doi.org/10.1016/j.jallcom.2021.159072.

[24] M.R. Manju, K.S. Ajay, Noel M. D'Souza, S. Hunagund, R.L. Hadimani, V. Dayal, Enhancement of ferromagnetic properties in composites of BaSnO3 and CoFe2O4, J. Magn. Magn. Mater. 452 (2018) 23–29, https://doi.org/10.1016/j.jmmm.2017.11.104.

[25] P.P. Khirade, Structural, microstructural and magnetic properties of sol–gel-synthesized novel BaZrO3–CoFe2O4 nanocomposite, J. Nanostruct. Chem. 9 (2019) 163–173, https://doi.org/10.1007/s40097-019-0307-8.

[26] P.P. Bardapurkar, S.S. Shewale, N.P. Barde, K.M. Jadhav, Structural, magnetic and catalytical properties of cobalt ferrite nanoparticles dispersed in silica matrix, Mater. Res. Express 6 (2019) 045055, https://doi.org/10.1088/2053-1591/aafe32.

[27] T. Dippong, O. Cadar, I.G. Deac, M. Lazar, G. Borodi, E.A. Levei, Influence of ferrite to silica ratio and thermal treatment on porosity, surface, microstructure and magnetic properties of Zn0.5Ni0.5Fe2O4/SiO2 nanocomposites, J. Alloy. Compd. 828 (2020) 154409, https://doi.org/10.1016/j.jallcom.2020.154409.

[28] T. Chen, J. Meng, Q. Lin, X. Wei, J. Li, Z. Zhang, One-step synthesis of hollow BaZrO3 nanocrystals with oxygen vacancies for photocatalytic hydrogen evolution from pure water, J. Alloy. Compd. 780 (2019) 498–503, https://doi.org/10.1016/j.jallcom.2018.11.367.

[29] P.P. Khirade, S.D. Birajdar, A.V. Humbe, K.M. Jadhav, Structural, electrical and dielectrical property investigations of Fe-doped BaZrO3 nanoceramics, J. Electron. Mater. 45 (2016) 3227–3235, https://doi.org/10.1007/s11664-016-4472-y.

[30] S. Parida, S.K. Rout, L.S. Cavalcante, E. Sinha, M.S. Li, V. Subramanian, N. Gupta, V.R. Gupta, J.A. Varela, E. Longo, Structural refinement, optical and microwave dielectric properties of BaZrO3, Ceram. Int. 38 (2012) 2129–2138, https://doi.org/10.1016/j.ceramint.2011.10.054.

[31] P.R. Choudhury, S.B. Krupanidhi, Dielectric response of BaZrO3/BaTiO3 and SrTiO3/BaZrO3 superlattices, J. Appl. Phys. 104 (2008) 114105, https://doi.org/10.1063/1.3031387.

[32] T. Dipponga, D. Tolomanb, E.-A. Leveic, O. Cadarc, A. Mesaros, A possible formation mechanism and photocatalytic properties of CoFe2O4/ PVA-SiO2 nanocomposites, Thermochim. Acta 666 (2018) 103–115, https://doi.org/10.1016/j.tca.2018.05.021.

[33] Y. Zhang, M. Zhu, Q. Zhang, H. Yu, Y. Li, H. Wang, Solvothermal one-step synthesis of MWCNTs/$Ni_{0.5}Zn_{0.5}Fe_2O_4$ magnetic composites, J. Magn. Magn. Mater. 322 (2010) 2006–2009, https://doi.org/10.1016/j.jmmm.2010.01.023.

[34] F.L. Zan, Y.Q. Ma, Q. Ma, G.H. Zheng, Z.X. Dai, M.Z. Wu, G. Li, Z.Q. Sun, X.S. Chen, One-step hydrothermal synthesis and characterization of high magnetization CoFe2O4/Co0.7Fe0.3 nanocomposite permanent magnets, J. Alloy. Compd. 553 (2013) 79–85, https://doi.org/10.1016/j.jallcom.2012.11.120.

[35] S. Farhat, R. Awad, Z. Bitar, Investigation of structural and magnetic properties of NiO/BaFe12O19/ Ni0.5Zn0.5Fe2O4 nanocomposites, Appl. Phys. A. 130 (2024) 446, https://doi.org/10.1007/s00339-024-07585-6.

[36] N.A. Algarou, Y. Slimani, M.A. Almessiere, A. Baykal, S. Guner, A. Manikandan, I. Ercan, Enhancement on the exchange coupling behavior of SrCo0.02Zr0.02Fe11.96O19/MFe2O4 (M = Co, Ni, Cu, Mn and Zn) as hard/soft magnetic nanocomposites, J. Magn. Magn. Mater. 499 (2020) 166308, https://doi.org/10.1016/j.jmmm.2019.166308.

[37] J. Guan, C. Zhang, H. Shao, H. Jiang, Y. Zhang, H. Xia, Jue Hu, Features of sonochemistry and its application in electrocatalyst synthesis, J. Alloy. Compd. 957 (2023) 170369, https://doi.org/10.1016/j.jallcom.2023.170369.

[38] M. Matar, O. Neamatallah, R. Awad, E.M. El-Maghraby, A.I. Abou-Aly, A. Khalaf, Identification of structural, optical, magnetic, and dielectric properties of (1-x) Ba0.5Sr0.5Fe12O19/(x)SnFe2O4, J. Alloy. Compd. 1041 (2025) 183703, https://doi.org/10.1016/j.jallcom.2025.183703.

[39] L. Shirmohammadzadeh, H.F. Moafi, A.F. Shojaei, Highly efficient Ag-doped Ba0.5Sr0.5ZrO3 nanocomposite with enhanced photocatalytic and antibacterial activity, J. Clust. Sci. 33 (2022) 1475–1488, https://doi.org/10.1007/s10876-021-02071-y.

[40] N.A. Algarou, Y. Slimani, M. A. Almessiere, A. Baykal, Exchange-coupling behavior in SrTb0.01Tm0.01Fe11.98O19/(CoFe2O4)x hard/soft nanocomposites, New J. Chem. 44 (2020) 5800–5808, https://doi.org/10.1039/D0NJ00109K.

[41] C.S. Munnolli, S.S. Kammar, V.K. Barote, A.A. Ibrahim, K.M. Batoo, S.E. Shirsath, R.H. Kadam, S.S. More, Thorough investigation of functional properties of ferroelectric (Bi0.5Na0.5TiO3)0.94-(BaTiO3)0.06 and hexaferrite SrCe0.05Sm0.05Fe11.9O19 composites, J. Magn. Magn. Mater. 607 (2024) 172396, https://doi.org/10.1016/j.jmmm.2024.172396.

[42] D.E. Bakeer, A.-H. Sakr, H.A. Motaweh, W. El-Sokary, An efficient co-precipitation synthesis of BaZr1-xCoxO3 nanoparticles: structural, optical and magnetic properties, J. Nanostruct. 9 (2019) 414–428, https://doi.org/10.22052/JNS.2019.03.003.

[43] R. Topkaya, Effect of Zn substitution on temperature dependent magnetic properties of BaFe12O19 hexaferrites, J. Alloy. Compd. 725 (2017) 1230–1237, https://doi.org/10.1016/j.jallcom.2017.07.248.

[44] Ab Kumar, R.K. Singh, H.K. Satyapal, Monalisa, Am Kumar, S. Sharma, Lattice strain mediated structural and magnetic properties enhancement of strontium hexaferrite nanomaterials through controlled annealing, Physica B 600 (2021) 412592, https://doi.org/10.1016/j.physb.2020.412592.

[45] M. Xu, Ch Cai, Y. Shi, M. Xie, Y. Wu, Y. Liu, J. Peng, J. Bao, S. An, The grain growth control of ZnO-V2O5 based varistors by PrMnO3 addition, Micromachines 13 (2022) 214, https://doi.org/10.3390/mi13020214.

[46] S.L. Hu, J. Liu, H.Y. Yu, Z.W. Liu, Synthesis and properties of barium ferrite nano-powders by chemical co-precipitation method, J. Magn. Magn. Mater. 473 (2019) 79–84, https://doi.org/10.1016/j.jmmm.2018.10.044.

[47] R.B. Jotania, R.A. Nandotaria, C.C. Chauhan, M. Hashim, S.S. Meena, S.E. Shirsath, Structural phases and Maxwell–Wagner relaxation in magnetically soft-ZnFe2O4 and hard-Sr2Cu2Fe12O22 nanocomposites, Ceram. Int. 42 (2016) 2289–2298, https://doi.org/10.1016/j.ceramint.2015.10.023.

[48] S. Keshri, L. Joshi, S.K. Rout, Influence of BTO phase on structural, magnetic and electrical properties of LCMO, J. Alloy. Compd. 485 (2009) 501–506, https://doi.org/10.1016/j.jallcom.2009.06.006.

[49] T.R. Aldhafeeri, S. Altaf, A.M. Fallatah, M.M. Baig, A. Alhadhrami, A.S. Almalki, U. Rafiq, S.G. Lee d, M.F. Warsi, Effective photodegradation of levofloxacin and amoxicillin using M-type Mg-Al-co-doped BaFe12O19 hexaferrite anchored onto the carbon nanotubes, Surf. Interfaces 76 (2025) 107876, https://doi.org/10.1016/j.surfin.2025.107876.

[50] N. Masunga, B.B. Mamba, Y.W. Getahun, A.A. El-Gendy, K.K. Kefeni, Synthesis of single-phase superparamagnetic copper ferrite nanoparticles using an optimized coprecipitation method, Mater. Sci. Eng. B 272 (2021) 115368, https://doi.org/10.1016/j.mseb.2021.115368.

[51] A. Bahadur, A. Saeed, S. Iqbal, M. Shoaib, I. Ahmad, M.S. Rahman, M.I. Bashir, M. Yaseen, W. Hussain, Morphological and magnetic properties of $BaFe_{12}O_{19}$ nanoferrite: a promising microwave absorbing material, Ceram. Int. 43 (2017) 7346–7350, https://doi.org/10.1016/j.ceramint.2017.03.039.

[52] C. Chinnusamy, R. Thiyagarajan, Mn-doped barium zirconate nanoparticles for high-performance photocatalyst applications, Physica B 718 (2025) 417868, https://doi.org/10.1016/j.physb.2025.417868.

[53] P. Hong, Y. Li, J. He, A. Saeed, K. Zhang, C. Wang, L. Kong, J. Liu, Rapid degradation of aqueous doxycycline by surface CoFe2O4/H2O2 system: behaviors, mechanisms, pathways and DFT calculation, Appl. Surf. Sci. 526 (2020) 146557, https://doi.org/10.1016/j.apsusc.2020.146557.

[54] S.M. Patange, S.E. Shirsath, S.P. Jadhav, V.S. Hogade, S.R. Kamble, K.M. Jadhav, Elastic properties of nanocrystalline aluminum substituted nickel ferrites prepared by co-precipitation method, J. Mol. Struct. 1038 (2013) 40–44, https://doi.org/10.1016/j.molstruc.2012.12.053.

[55] M.M. Barakat, D.E. Bakeer, A.-H. Sakr, Structural, magnetic properties and electron paramagnetic resonance for BaFe12-xHgxO19 hexaferrite nanoparticles prepared by co-precipitation method, J. Taibah Univ. Sci. 14 (2020) 640–652, https://doi.org/10.1080/16583655.2020.1761676.

[56] K.S. Knight, Low-temperature thermophysical and crystallographic properties of BaZrO3 perovskite, J. Mater. Sci. 55 (2020) 6417–6428, https://doi.org/10.1007/s10853-020-04453-5.

[57] R. Terki, G. Bertrand, H. Aourag, C. Coddet, Thermal properties of Ba1−xSrxZrO3 compounds from microscopic theory, J. Alloy. Compd. 456 (2008) 508–513, https://doi.org/10.1016/j.jallcom.2007.02.133.
[58] S.D. Ghongade, M.D. Patil, M.R. Waikar, A.R. Sonkawade, A.M. Bagwan, S. J. Shinde, A.V. Moholkar, R.G. Sonkawade, Unveiling elegant in-situ properties: structure and vibrations of the polymer solution synthesised BaFe12O19, Surf. Interfaces 53 (2024) 105005, https://doi.org/10.1016/j.surfin.2024.105005.
[59] J. Kreisel, G. Lucazeau, H. Vincent, Raman spectra and vibrational analysis of BaFe12O19 hexagonal ferrite, J. Solid State Chem. 137 (1998) 127–137, https://doi.org/10.1006/jssc.1997.7737.
[60] S. Gulbadan, M.A. Khan, G.A. Ashraf, K. Mahmood, M. Shahid, M. Irfan, A. Ahmad, Insight of structural, dielectric and spectroscopic characteristics of Ba0.6Sr0.4-xYbxFe12-yCoyO19 M-type hexaferrite, Ceram. Int. 49 (2023) 6487–6499, https://doi.org/10.1016/j.ceramint.2022.10.162.
[61] W.Y. Zhao, P. Wei, X.Y. Wu, W. Wang, Q.J. Zhang, Lattice vibration characterization and magnetic properties of M-type barium hexaferrite with excessive iron, J. Appl. Phys. 103 (2008) 063902, https://doi.org/10.1063/1.2884533.
[62] F.M.S. Junior, C.W.A. Paschoal, Spin-phonon coupling in BaFe12O19 M-type hexaferrite, J. Appl. Phys. 116 (2014) 244110, https://doi.org/10.1063/1.4904062.
[63] X.-Bai Chen, T.M. Hien Nguyen, K. Han, J.C. Sur, N.H. Sung, B.K. Cho, I.-S. Yang, Raman studies of spin-phonon coupling in hexagonal BaFe12O19, J. Appl. Phys. 114 (2013) 013912, https://doi.org/10.1063/1.4812575.
[64] T.N. Stanislavchuk, A.A. Sirenko, A.P. Litvinchuk, X. Luo, S.-W. Cheong, Electronic band structure and optical phonons of BaSnO3 and Ba0.97La0.03SnO3 single crystals: theory and experiment, J. Appl. Phys. 112 (2012) 044108, https://doi.org/10.1063/1.4748309.
[65] C. Toulouse, D. Amoroso, C. Xin, P. Veber, M.C.H.G. Balakrishnan, M. Maglione, P. Ghosez, J. Kreisel, M. Guennou, Lattice dynamics and Raman spectrum of BaZrO3 single crystals, Phys. Rev. B 100 (2019) 134102, https://doi.org/10.48550/arXiv.1907.02008.
[66] R. Kurre, S. Bajpai, P.K. Bajpai, Synthesis, characterization, optical and transport properties of BaSnO3 synthesized by wet chemical route, Mater. Sci. Appl. 9 (2018) 92–110, https://doi.org/10.4236/msa.2018.91007.
[67] E.C. Aguiar, A.Z. Simoes, C.A. Paskocimas, M. Cilense, E. Longo, J.A. Varela, Photoluminescence of BaZrO3 explained by a order/disorded transformation, J. Mater. Sci. Mater. Electron. 26 (2015) 1993–2001, https://doi.org/10.1007/s10854-015-2701-4.
[68] M. Karlsson, A. Matic, C.S. Knee, I. Ahmed, S.G. Eriksson, L. Börjesson, Short-range structure of proton-conducting perovskite BaInxZr1−xO3−x/2 (x = 0–0.75), Chem. Mater. 20 (2008) 3480–3486, https://doi.org/10.1021/cm7025448.
[69] N.K. Karan, R.S. Katiyar, T. Maiti, R. Guo, A.S. Bhalla, Raman spectral studies of Zr4+- rich BaZrxTi1−xO3 ($0.5 \leq x \leq 1.00$) phase diagram, J. Raman Spectrosc. 40 (2009) 370–375, https://doi.org/10.1002/jrs.2134.
[70] C. Xin, P. Veber, M. Guennou, C. Toulouse, N. Valle, M.C. Hatnean, G. Balakrishnan, Single crystal growth of BaZrO3 from the melt at 2700 °C using optical floating zone technique and growth prospects from BaB2O4 flux at 1350 °C, Cryst. Eng. Comm. 21 (2019) 502, https://doi.org/10.1039/c8ce01665h.
[71] F. Shi, H. Dong, Q. Liu, J. Yang, S. Ren, H. Sun, J. Xiong, Investigation and theoretical calculation of the lattice vibrational spectra of BaZrO3 ceramic, J. Mater. Sci. Mater. Electron. 28 (2017) 3467–3473, https://doi.org/10.1007/s10854-016-5944-9.
[72] D. El-Said Bakeer, M.Y. El Sayed, E.M. Abdallah, R. Awad, S.G. Elsharkawy, Structural and magnetic tailoring of Co-Cu ferrite nanoparticles via Cd^{2+} substitution: a multi characterization approach, Appl. Phys. A 131 (2025) 885, https://doi.org/10.1007/s00339-025-08897-x.
[73] S. Vadivelan, N.J. Victor, Investigation of magnetic and structural properties of copper substituted barium ferrite powder particles via co-precipitation method, Results Phys. 6 (2016) 843–850, https://doi.org/10.1016/j.rinp.2016.07.013.
[74] T. Xie, L. Xu, C. Liu, Dielectric and magnetic response of Sr–Zn ferrite composite, RSC Adv. 3 (2013) 15856–15865, https://doi.org/10.1039/C3RA41361F.
[75] L. Wangn, J. Zhang, Q. Zhang, N. Xu, J. Song, XAFS and XPS studies on site occupation of Sm3+ ions in Sm doped M-type BaFe12O19, J. Magn. Magn. Mater. 377 (2015) 362–367, https://doi.org/10.1016/j.jmmm.2014.10.097.
[76] Y. Zhang, P. Wang, H. Zhou, X. Zhan, Z. Wei, Z. Yin, Z. Wang, Z. Wang, Excavating oxygen vacancies in BaZrO3 to boost photocatalysis via screening vantage crystal planes, Appl. Catal. B: Environ. Energy 361 (2025) 124633, https://doi.org/10.1016/j.apcatb.2024.124633.
[77] D. Fernandes, P.G. Hernandes, R.D. Carvalho, I.L. Rodrigues, C.W. Raubach, M. L. Moreira, P.L.G. Jardim, M.M. Ferrer, E.C. Moreira, V.R. Mastelaro, C.Fde O. Graeff, S. da S. Cava, BaZrO3 and its application as a photocatalyst for Rhodamine B removal, Chem. Phys. Lett. 856 (2024) 141633, https://doi.org/10.1016/j.cplett.2024.141633.
[78] T. Garg, Movikiran, Nitansh, P. Kaur, S. Singhal, Heterogeneous photo-Fenton like S, Cl co-doped g-C3N4/SrFe12O19 heterojunction for enhanced photocatalytic degradation of fluoroquinolones antibiotics, Diam. Relat. Mater. 158 (2025) 112696, https://doi.org/10.1016/j.diamond.2025.112696.
[79] M. Yousaf, S. Nazir, Q. Hayat, M.N. Akhtar, M. Akbar, Y. Lu, A. Noor, J.-M. Zhang, M.A.K.Y. Shah, B. Wang, Magneto-optical properties and physical characteristics of M-type hexagonal ferrite (Ba1-xCaxFe11.4Al0.6O19) nanoparticles (NPs), Ceram. Int. 47 (2021) 11668–11676, https://doi.org/10.1016/j.ceramint.2021.01.006.
[80] H. Irfan, R.E. Vizhi, Enhancement of the maximum energy product in $Ba_{0.5}Sr_{0.5}Fe_{12}O_{19}/Y_3Fe_5O_{12}$ nanocomposites synthesized by the co-precipitation method, Nanotechnology 31 (2020) 404001, https://doi.org/10.1088/1361-6528/ab9260.
[81] V. Harikrishnan, R.E. Vizhi, Temperature-dependent phase transition: structural and magnetic properties of Ba0.5Sr0.5Fe12O19-CoFe2O4 nanocomposites, J. Phys. Chem. Solids 127 (2019) 35–42, https://doi.org/10.1016/j.jpcs.2018.12.004.
[82] R.E. Vizhi, V. Harikrishnan, P. Saravanan, D.R. Babu, Influence of Co-substitution on structural and magnetic properties of nanocrystalline Ba0.5Sr0.5Fe12O19, J. Cryst. Growth 452 (2016) 117–124, https://doi.org/10.1016/j.jcrysgro.2016.01.026.
[83] M.A. Wahba, S.M. Yakout, Innovative visible light photocatalytic activity for V-doped ZrO2 structure: optical, morphological, and magnetic properties, J. Sol-Gel Sci. Technol. 92 (2019) 628–640, https://doi.org/10.1007/s10971-019-05103-2.
[84] V. Ratchagar, K. Jagannathan, Synthesis and characterization of highly efficient ZrO2 nanomaterials for electrochemical behaviour, J. Supercond. Nov. Magn. 33 (2020) 3433–3441, https://doi.org/10.1007/s10948-020-05592-1.
[85] E. Brand, V. Rosendal, Y. Wu, T. Tran, A. Palliotto, I.V. Maznichenko, S. Ostanin, V. Esposito, A. Ernst, S. Zhou, D.-S. Park, N. Pryds, Defect-induced magnetic symmetry breaking in oxide materials, Appl. Phys. Rev. 12 (2025) 011327, https://doi.org/10.1063/5.0216796.
[86] C.C. Chauhan, A.R. Kagdi, R.B. Jotania, A. Upadhyay, C.S. Sandhu, S.E. Shirsath, S. S. Meena, Structural, magnetic and dielectric properties of Co-Zr substituted M-type calcium hexagonal ferrite nanoparticles in the presence of α-Fe2O3 phase, Ceram. Int. 44 (2018) 17812–17823, https://doi.org/10.1016/j.ceramint.2018.06.249.
[87] M.N. Akhtar, S. Javed, M. Ahmad, A. Sulong, M.A. Khan, Sol gel derived MnTi doped Co2 W-type hexagonal ferrites: structural, physical, spectral and magnetic evaluations, Ceram. Int. 46 (2020) 7842–7849, https://doi.org/10.1016/j.ceramint.2019.12.003.
[88] Au Rashid, A. Humayun, S. Manzoor, MgFe2O4/ZrO2 composite nanoparticles for hyperthermia applications, J. Magn. Magn. Mater. 428 (2017) 333–339, https://doi.org/10.1016/j.jmmm.2016.12.119.
[89] T. Dippong, O. Cadar, E.A. Levei, I.G. Deac, Microstructure, porosity and magnetic properties of Zn0.5Co0.5Fe2O4/SiO2 nanocomposites prepared by sol-gel method using different polyols, J. Magn. Magn. Mater. 498 (2020) 166168, https://doi.org/10.1016/j.jmmm.2019.166168.
[90] B.J. Rodriguez, Y.H. Chu, R. Ramesh, S.V. Kalinin, Ferroelectric domain wall pinning at a bicrystal grain boundary in bismuth ferrite, Appl. Phys. Lett. 93 (2008) 142901, https://doi.org/10.1063/1.2993327.
[91] E.C. Stoner, E. Wohlfarth, A mechanism of magnetic hysteresis in hetrogenious alloy, Philos. Trans. A 240 (1948) 599–642, https://doi.org/10.1098/rsta.1948.0007.
[92] K. Sadhana, K. Praveena, S. Matteppanavar, B. Angadi, Structural and magnetic properties of nanocrystalline BaFe12O19 synthesized by microwave-hydrothermal method, Appl. Nanosci. 2 (2012) 247–252, https://doi.org/10.1007/s13204-012-0100-1.
[93] F. Máca, J. Kudrnovský, V. Drchal, G. Bouzerar, Magnetism without magnetic impurities in ZrO2 oxide, Appl. Phys. Lett. 92 (2008) 212503, https://doi.org/10.1063/1.2936858.
[94] M.A. Paulin, G. Alejandro, D.G. Lamas, M. Quintero, R.O. Fuentes, J.E. Gayone, A. Butera, A.G. Leyva, J. Sacanell, Oxygen vacancies and their role on the magnetic character of polycrystalline CeO2, Ceram. Int. 49 (2023) 5146–5153, https://doi.org/10.1016/j.ceramint.2022.10.031.
[95] E.C. Devi, I. Soibam, Law of approach to saturation in Mn–Zn ferrite nanoparticles, J. Supercond. Nov. Magn. 32 (2019) 1293–1298, https://doi.org/10.1007/s10948-018-4823-4.
[96] R. Pattanayak, R. Muduli, R.K. Panda, T. Dash, P. Sahu, S. Raut, S. Panigrahi, Investigating the effect of multiple grain-grain interfaces on electric and magnetic properties of [50 wt% BaFe12O19–50 wt%Na0.5Bi0.5TiO3] composite system, Phys. B Condens. Matter 485 (2016) 67–77, https://doi.org/10.1016/j.physb.2016.01.011.
[97] S. Narendra Babu, S. Gi Min, L. Malkinski, Electric field tunable magnetic properties of lead-free Na0.5Bi0.5TiO3/CoFe2O4 multiferroic composites, J. Appl. Phys. 109 (2011), https://doi.org/10.1063/1.3544500.
[98] C. Zhang, Y. Xie, Q. Zhan, Y. Hu, Anisotropic coercivity and the effects of interlayer exchange coupling in CoFeB/FeRh bilayers, Phys. Rev. B 103 (2021) 014445, https://doi.org/10.1103/PhysRevB.103.014445.
[99] B. Podmiljšak, B. Saje, P. Jenuš, T. Tomše, S. Kobe, K. Žužek, S. Šturm, The future of permanent-magnet-based electric motors: how will rare earths affect electrification? Materials 17 (2024) 848, https://doi.org/10.3390/ma17040848.